

# Structure of the outer layers of cool standard stars

S. Dehaes<sup>1</sup>, E. Bauwens<sup>2</sup>, L. Decin<sup>2,3\*</sup>, K. Eriksson<sup>4</sup>, G. Raskin<sup>2</sup>, B. Butler<sup>5</sup>, C.D. Dowell<sup>6</sup>, B. Ali<sup>7</sup>, and  
J.A.D.L. Blommaert<sup>2</sup>

<sup>1</sup> Department of Mathematics, K.U.Leuven, Celestijnenlaan 200B, B-3001 Leuven, Belgium

<sup>2</sup> Department of Physics and Astronomy, Institute for Astronomy, K.U.Leuven, Celestijnenlaan 200D, B-3001 Leuven, Belgium

<sup>3</sup> Sterrenkundig Instituut Anton Pannekoek, University of Amsterdam, Kruislaan 403 1098 Amsterdam, The Netherlands

<sup>4</sup> Department of Astronomy and Space Physics, Uppsala University, Box 515, SE-751 20 Uppsala, Sweden

<sup>5</sup> NRAO P.O. Box O, Socorro NM, 87801 USA

<sup>6</sup> Jet Propulsion Laboratory / California Institute of Technology, MS 169-506, 4800 Oak Grove Dr., Pasadena, CA 91109, USA

<sup>7</sup> IPAC / Caltech, MS 100-22, Pasadena, CA 91125, USA

Received; accepted

## Abstract

**Context.** Among late-type red giants, an interesting change occurs in the structure of the outer atmospheric layers as one moves to later spectral types in the Hertzsprung-Russell diagram: a chromosphere is always present, but the coronal emission diminishes and a cool massive wind steps in.

**Aims.** Where most studies have focussed on short-wavelength observations, this article explores the influence of the chromosphere and the wind on long-wavelength photometric measurements.

**Methods.** The observational spectral energy distributions are compared with the theoretical predictions of the MARCS atmosphere models for a sample of nine K- and M-giants. The discrepancies found are explained using basic models for flux emission originating from a chromosphere or an ionized wind.

**Results.** For 7 out of 9 sample stars, a clear flux excess is detected at (sub)millimeter and/or centimeter wavelengths, for the other two only observational upper limits are obtained. The precise start of the excess depends upon the star under consideration. The flux at wavelengths shorter than  $\sim 1$  mm is most likely dominated by an optically thick chromosphere, where an optically thick ionized wind is the main flux contributor at longer wavelengths.

**Conclusions.** Although the optical to mid-infrared spectrum of the studied K- and M-giants is well represented by a radiative equilibrium atmospheric model, the presence of a chromosphere and/or ionized stellar wind at higher altitudes dominates the spectrum in the (sub)millimeter and centimeter wavelength ranges. The presence of a flux excess also has implications on the role of these stars as fiducial spectrophotometric calibrators in the (sub)millimeter and centimeter wavelength range.

**Key words.** Stars: chromospheres – Stars: late-type – Stars: winds, outflows – Radio continuum: stars

## 1. Introduction

Several studies in the past three decades (see, e.g., Linsky & Haisch 1979; Ayres et al. 1981; Hünsch et al. 1996; Haisch et al. 1990) have revealed the existence of dividing lines in the cool half of the Hertzsprung-Russell (HR) diagram, where the giants and supergiants reside. These dividing lines are based on differences in the physics of the outer atmospheric layers. To the blue side of the dividing lines, the late-type stars are surrounded by chromospheres and coronae. To the red side the stars also possess chromospheres, but in combination with a cool stellar wind. At the time of the introduction of the dividing lines (Linsky & Haisch 1979; Ayres et al. 1981) there

were no observational indications for the presence of a corona on the red side, nowadays there is evidence for some coronal emission, although much weaker than on the blue side of the dividing lines (Ayres et al. 1997).

Most studies of these outer stellar layers have focussed on X-ray and UV observations. But the far-infrared (FIR) continuum can also be used as a probe of the layers of the atmosphere for solar and cooler stars. As the primary infrared (IR) continuum opacity, coming from free-free processes, increases with the square of wavelength, we see emission from increasingly outer lying layers the longer the wavelength we observe.

In this study, we use (sub)millimeter and centimeter wavelength observations to gain further insight into the outer structure of nine giants of spectral type K and M. The selected stars are ‘standard’ stars, used in the calibration pedigree of many IR spectroscopic and photometric instruments. All of them belong

Send offprint requests to: S. Dehaes, e-mail: sofie.dehaes@wis.kuleuven.be

\* Postdoctoral Fellow of the Fund for Scientific Research, Flanders

**Table 1.** Some characteristics of the sample stars. The values for  $M_{bol}$  are taken from Decin et al. (2003a), Kashyap et al. (1994) and Eggen & Stokes (1970). No uncertainties were given in these articles on the values of  $M_{bol}$  for  $\iota$  Aur and  $\sigma$  Lib.

	spectral type	$M_{bol}$	$B - V$
$\alpha$ Boo	K2 IIIp	$-0.90 \pm 0.05$	1.23
$\alpha$ Cet	M2 III	$-3.09 \pm 0.13$	1.66
$\alpha$ Tau	K5 III	$-1.72 \pm 0.06$	1.54
$\beta$ And	M0 III	$-3.14 \pm 0.11$	1.58
$\beta$ Peg	M2.5 III	$-3.34 \pm 0.11$	1.67
$\gamma$ Dra	K5 III	$-2.07 \pm 0.07$	1.52
$\beta$ UMi	K4 III	$-1.71 \pm 0.07$	1.51
$\iota$ Aur	K3 II	-2.4	1.55
$\sigma$ Lib	M3/M4 III	-3.6	1.65

to the group of stars with no or low coronal activity. With the launch of the ESA-satellite Herschel, which covers the full 55 to 672  $\mu\text{m}$  wavelength range, it is of interest to study whether these low-activity stars can also be used as calibrators at these far-infrared wavelengths. In Sect. 2 the selection criteria for the stars are outlined. Data reduction for the different data-sets is presented in Sect. 3. Sect. 4 confronts the spectral energy distributions (SEDs) of the stars with the hydrostatic MARCS atmosphere models. In Sect. 5, the discrepancies found in the previous section are discussed. The conclusions are given in Sect. 6.

## 2. Sample selection

The stars in our sample are part of a larger set of standard stars used for the spectrophotometric calibration of near- and mid-infrared instruments (Decin et al. 2003b,c,a, 2004; Decin & Eriksson 2007; Gordon et al. 2007). They are selected for their low chromospheric and coronal activity (see, e.g., Wiedemann et al. 1994; O'Brien & Lambert 1986, and further in Sect. 5.4 an 5.3). The position of our sample stars in the HR-diagram indicates that they have low coronal activity, however, it also points to the presence of a cool stellar wind. These stars are potential candidates to be selected as fiducial calibration sources for the PACS (60 – 210  $\mu\text{m}$ ) and SPIRE (200 – 670  $\mu\text{m}$ ) instruments, which are onboard the ESA Herschel-satellite. Hence, it is necessary to check if the possible presence of a chromosphere, corona or stellar wind causes a flux excess in the far-infrared, although they are not visible in the near-infrared CO lines (Wiedemann et al. 1994). Some characteristics of the selected stars are given in Table 1.

## 3. Observations and data reduction

To construct the SEDs of each of the standard stars several photometric data points were gathered from the literature. We have used the UBVRJIKLMNH Photoelectric Catalogue (Morel & Magnenat 1978), the Revised AFGL (RAFGL) Catalogue (Price & Murdock 1983), the IRAS catalogue of Point Sources (IRAS PSC), Version 2.0 (Beichman et al. 1988), observations in the Geneva Photometric System 4 (Rufener 1989), radio continuum data from Wendker (1995)

**Table 2.** Fluxes at 1.2 mm determined from SIMBA observations. Also listed are the ideal aperture used and the rms noise on the sky background. The given uncertainty does not take the uncertainty on the absolute calibration into account.

target	flux (mJy)	ideal aperture (arcsec)	rms (mJy)
$\alpha$ Boo	$105.6 \pm 6.9$	45	8.4
$\beta$ And	< 40.1		13.8
$\alpha$ Cet	$58.3 \pm 4.1$	55	6.0
$\beta$ Peg	$29.2 \pm 2.5$	20	6.6

and Cohen et al. (2005), photometric data in the Johnson's 11-color system (Ducati 2002), the COBE DIRBE Point Source Catalog (Smith et al. 2004) and the 2MASS All-Sky Catalog of Point Sources (Skrutskie et al. 2006). A summary of the available data can be found in Tables A.1 – A.5 in the on-line appendix. In order to study the outer atmospheric layers, (sub)millimeter and centimeter data have been obtained with (1.) the SIMBA bolometer array at 1.2 mm at the SEST telescope, (2.) the MAMBO II bolometer array at 1.2 mm on the IRAM telescope, (3.) the SHARC II camera at 350  $\mu\text{m}$  and 450  $\mu\text{m}$  on the CSO, and (4.) the VLA at 22 and 43.3 GHz. The reduction of each of these newly obtained data-sets is shortly discussed in the next paragraphs.

### 3.1. SIMBA observations

$\alpha$  Boo,  $\beta$  And,  $\alpha$  Cet and  $\beta$  Peg were observed with SIMBA (2003 July 13 – 15) at 1.2 mm, using the fast-scanning technique. The MOPSI<sup>1</sup> software developed by R. Zylka was used for the data reduction. In a first reduction step, some fundamental operations like despiking, opacity correction and sky-noise reduction are performed on each scan. Once the scans made during different nights are assembled, the position of the source is more accurately determined, which can be used for baseline definition and for improvement of the sky-noise reduction. For the absolute calibration, scans of Uranus were used. The model for Uranus is the standard model offered by MOPSI, the calibration uncertainties are estimated at 15%. After the data reduction, fluxes were determined using aperture photometry. For each source, the 'ideal' aperture was determined, being the aperture with the highest corresponding signal-to-noise ratio. A more vast description of the data reduction and analysis of the SIMBA data is given in Dehaes et al. (2007). Table 2 shows the determined fluxes together with the ideal aperture used and the rms noise on the sky background.

### 3.2. MAMBO II observations

Observations at 1.2 mm with MAMBO II were obtained for  $\alpha$  Boo,  $\iota$  Aur,  $\beta$  UMi,  $\gamma$  Dra,  $\alpha$  Tau,  $\beta$  And,  $\alpha$  Cet,  $\beta$  Peg and  $\sigma$  Lib (2003 October-November). The reduction was done with

<sup>1</sup> Observers Handbook SIMBA, 2003, edition 1.9, <http://www.ls.eso.org/lasilla/Telescopes/SEST/html/telescope-instruments/simba/index>

**Table 3.** Fluxes at 1.2 mm determined from MAMBO II observations.  $\alpha$  Tau is not listed here, since the uncertainty on the measurement was too large to give any restraints. The observations of  $\alpha$  Boo and  $\alpha$  Cet are discarded in the subsequent analysis (see Sect. 3.2 for explanation).

target	flux (mJy)
$\alpha$ Boo	$20.8 \pm 3.5$
$\iota$ Aur	$5.5 \pm 1.6$
$\beta$ UMi	$12.2 \pm 1.6$
$\gamma$ Dra	$10.1 \pm 1.3$
$\beta$ And	$23.5 \pm 2.7$
$\alpha$ Cet	$23.6 \pm 2.5$
$\beta$ Peg	$29.5 \pm 3.2$
$\sigma$ Lib	$12.1 \pm 2.0$

an adjusted version of the MOPSI software called MOPSI<sup>2</sup>, using the standard scripts provided for the reduction of On-Off data. These scripts also include standard reduction steps such as baseline fitting, despiking, correlated skynoise filtering, etc. Flux calibration is done using a default conversion factor provided by MOPSI, the calibration uncertainties are estimated at 15%. After these reduction steps, scans of the same source are combined to give one result. Table 3 lists the determined fluxes. For 4 sources both SEST and IRAM data were available. Both measurements coincide for  $\beta$  Peg and the upper limit determined from the SIMBA observations is in agreement with the flux measured by MAMBO II for  $\beta$  And. For  $\alpha$  Boo and  $\alpha$  Cet, the 2 measurements do not agree within the errors. As the MAMBO II observations were performed in service mode and the log-files state very unstable weather conditions for  $\alpha$  Cet and altocumulus clouds right after the observation of  $\alpha$  Boo, we have more confidence in the results from the SIMBA observations (which were performed in visitor mode). For  $\alpha$  Boo and  $\alpha$  Cet the MAMBO II observations are discarded for the remainder of the article. Since the MAMBO II observations for the other objects are in good agreement with the SIMBA data (e.g.  $\beta$  Peg), with data from the catalogs (e.g.  $\beta$  And) and since measurements at these long wavelengths are scarce, the data are retained for the other objects.

### 3.3. CSO observations

Observations of five giant stars were made at  $350 \mu\text{m}$  and  $450 \mu\text{m}$  using the SHARC II camera at Caltech Submillimeter Observatory on several nights in 2005 and 2008. Standard Lissajous scans were used for the stars and calibrators. The weather conditions were favorable: clear skies, low humidity, and precipitable water vapor in the range 1 – 2 mm. Occasional periods of unstable atmospheric transmission appear to have been properly accounted for in the data analysis. Instead of using the facility 225 GHz radiometer for atmospheric extinction correction, we used (for each observation in Table 4) the tight correlation between the observed signals from the calibrators (in raw V) and the average full DC voltage of the bolometers

at the time of the observations to calculate a calibration factor which was then applied to the target star. The full DC bolometer voltage is responsive to the emission from the atmosphere and therefore its transparency. In the analysis, the detectors were corrected for their slight nonlinear response. The beam size of CSO/SHARC II at  $350$  and  $450 \mu\text{m}$  is  $8.3 \pm 0.3$  arcsec and  $9.8 \pm 0.3$  arcsec, respectively, and all of the giant stars are unresolved. The calibrators are unresolved or only slightly resolved.

The absolute flux calibration is based on the Wright (1976) model for Mars and subsequent planet observations and analysis by Griffin & Orton (1993). From this work, the absolute uncertainties in the fluxes of Uranus and Neptune are believed to be 5%. Our submillimetre observations of  $\beta$  Peg are calibrated directly vs. Uranus and Neptune and are assigned a systematic calibration uncertainty of 10% in Table 4. For the remaining sources, we used secondary calibrators having fluxes tabulated by Sandell (1994), G. Sandell (priv. comm.), Jenness et al. (2002), the JCMT/SCUBA flux calibration web site (2005 update), and our own cross calibration work. Our best estimates for the secondary calibrator fluxes are given in the table, and the target stars calibrated with respect to them are assigned a systematic uncertainty of 15%. In several cases, the statistical uncertainties are much smaller than the systematic uncertainties, so these measurements would benefit from an improved knowledge of the fluxes of the secondary calibrators.

### 3.4. VLA observations

The VLA (Very Large Array) measurements were taken in two bands: the Q-band (6.9 cm) and the K-band (1.3 cm). In all of our observations, we observed in the continuum mode, which effectively provides measurements of the total intensity (Stokes I) with an equivalent bandwidth of  $\sim 184$  MHz<sup>3</sup>. The observations for  $\alpha$  Boo were undertaken on two separate occasions - on January 6, 1999, and on January 25, 2004, for  $\beta$  Peg on April 21, 2005. For the 1999 experiment, the VLA was in the C configuration, with maximum physical antenna separation of  $\sim 3.4$  km. At this time, only about half of the antennas were equipped with Q-band receivers and during our experiment 12 were available for this frequency. The other 15 were tuned to K-band for simultaneous observations. The  $\alpha$  Boo observations were part of a larger program to observe possible sources for millimeter wavelength flux calibration that time, and as such were limited to only about an hour in extent. For the 2004 and 2005 experiments, the VLA was in the B configuration, with maximum physical antenna separation of  $\sim 11.4$  km. A full 6 hour observation was dedicated to the star at Q-band.

Subsequent calibration of the data proceeded in the normal fashion for VLA data, in the AIPS reduction package (<http://www.cv.nrao.edu/aips/>). For all data, the absolute flux density scale was set with an observation of 3C286, with as-

<sup>3</sup> The VLA receivers actually operate in the two orthogonal circular polarizations, with 92 MHz bandwidth in each polarization. Since for  $\alpha$  Boo and  $\beta$  Peg, we expect the two circular polarizations to have equal intensity, they are combined into a total intensity polarization (Stokes I), for an effective increase of 2 to the bandwidth, yielding 184 MHz equivalent bandwidth.

<sup>2</sup> <http://www.iram.es/IRAMES/mainWiki/CookbookMopsic>

**Table 4.** CSO observations at 350  $\mu\text{m}$  and 450  $\mu\text{m}$ .

Star	Wavelength ( $\mu\text{m}$ )	Flux (mJy)	Statistical Uncertainty (mJy)	Systematic Uncertainty (mJy)	Observing Dates	Calibrator Fluxes (Jy/beam)
$\alpha$ Boo	350	601	35		2005 May 10-13	Arp 220 (10.5)
		538	53		2008 Mar 1	Arp 220 (10.5)
		507	19		2008 May 28	Arp 220 (10.5)
		529	27	79	average	
$\alpha$ Boo	450	488	48		2008 Mar 2	Arp 220 (5.4)
		440	11		2008 Apr 7	Arp 220 (5.4)
		442	11	66	average	
$\alpha$ Cet	350	210	16	32	2008 Sep 22	Vesta (11.3)
$\alpha$ Cet	450	110	28	17	2008 Sep 24	Vesta (7.1)
$\alpha$ Tau	350	530	20	80	2008 Sep 17-18	Vesta (10.8), Pallas (9.5)
$\alpha$ Tau	450	304	39	46	2008 Sep 24	Vesta (7.2), CRL 618 (11.8), HL Tau (10.4)
$\beta$ Peg	350	361	9	36	2008 Sep 22	Uranus (234), Neptune (92), CRL 2688 (49)
$\beta$ Peg	450	240	12	24	2008 Sep 23-24	Uranus (169), CRL 2688 (26.8)
$\gamma$ Dra	350	116	25	17	2008 Sep 22,24	CRL 2688 (49)

sumed flux densities of 1.455 and 2.520 Jy for Q- and K-bands, respectively. Uncertainties in this flux density scale are  $\sim 10\%$  at Q-band and  $5\%$  at K-band. Observations of the unresolved secondary calibrator J1357+193 were used to remove long timescale (minutes) atmospheric and system fluctuations in the data. The derived flux densities of J1357+193 were 0.668 and 0.835 Jy at Q- and K-bands in 1999, and 1.175 Jy at Q-band in 2004 (the level of variation is common with these point-like calibration QSOs at radio wavelengths).

Images were then constructed from the visibilities via standard AIPS routines. The images were lightly CLEANed (a few  $10^3$ 's of components) to remove the sampling pattern of the array from them. The final total flux density was then calculated in five different ways: (1.) by counting up the flux density in the CLEAN components; (2.) by taking the peak flux density in the image; (3.) by counting up the flux density around the central location in the image; (4.) by fitting a gaussian to the image, and taking the peak of that fit gaussian (we do not actually resolve the star); and (5.) by actually fitting the visibilities themselves to find the flux density of a point source near the image center. The final estimated flux density is taken as the median of these five estimates. The uncertainty is taken as the average of the uncertainty from the image and visibility fits. This is only the formal uncertainty, systematic uncertainties must be considered in addition to this. These can arise from: inaccurate flux density scale, bad pointing, bad elevation corrections, atmospheric decorrelation, other electronics sources. Of these, by far the dominant uncertainty is the flux density scale, as the others are accounted for in various ways in the calibration.

Table 5 shows the resultant flux densities and uncertainties (formal only) for the VLA observations. The two observations of  $\alpha$  Boo at Q-band are consistent with each other, and the K-band observation in 1999 is also consistent, given the expected spectral index.

**Table 5.** Final flux densities from VLA observations of  $\alpha$  Boo and  $\beta$  Peg. The given uncertainty does not take the uncertainty on the absolute calibration into account.

target	date	frequency GHz	wavelength cm	flux density mJy
$\alpha$ Boo	1999-Jan-06	22.46	6.9	$1.7 \pm 0.2$
$\alpha$ Boo	1999-Jan-06	43.30	1.3	$3.3 \pm 0.4$
$\alpha$ Boo	2004-Jan-25	43.30	1.3	$3.34 \pm 0.08$
$\beta$ Peg	2005-Apr-21	43.30	1.3	$2.49 \pm 0.12$

#### 4. Comparison between SED and theoretical predictions

The observational SEDs are compared with the theoretical predictions of the SOSMARCS code of Plez et al. (1992), which is a refined version of the original MARCS code of Gustafsson et al. (1975). The synthetic spectra were computed with TURBOSPECTRUM (Plez et al. 1992), the improved version of the SPECTRUM program. For an overview of the continuum and line opacity lists used, we refer to Decin (2000). The MARCS model atmosphere code is built on the assumptions of local thermodynamic equilibrium, spherical or plane-parallel stratification in homogeneous stationary layers and hydrostatic equilibrium.

The geometry of the radiation transfer problem for the K- and M-giants in our sample was given by spherically symmetric layers. Since the MARCS model atmosphere only extends up to 200  $\mu\text{m}$ , the far-infrared continuum spectrum was computed by extrapolation from the continuum theoretical spectrum between 50 and 200  $\mu\text{m}$ . We therefore have determined the temperature of the flux forming region where  $\tau_\lambda = 1$ , with  $\lambda$  ranging from 50 to 200  $\mu\text{m}$ . With  $\text{H}^-$  free-free being the main continuum opacity source, subsequent outer cooler layers are sampled for longer wavelengths. Using a logarithmic

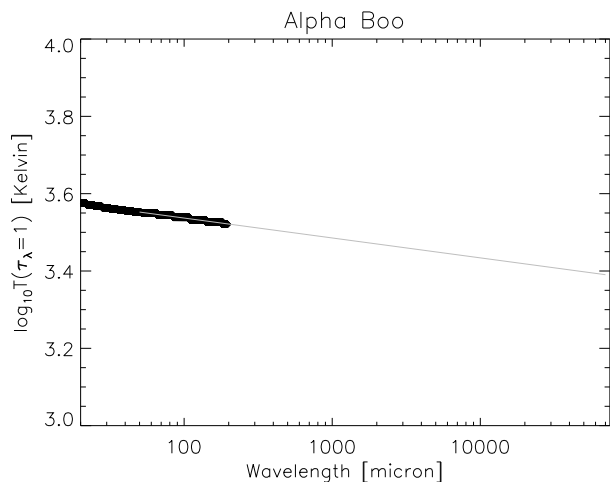


**Figure 1.** Temperature of the atmospheric model layer where  $\tau_\lambda = 1$  for wavelengths between 20 and 200  $\mu\text{m}$  (black thick line) for  $\alpha$  Boo. The temperature of the characteristic layer where most of the photospheric flux is formed ( $T_{(\tau_\lambda=1)}$ ) for the full 200 to 7500  $\mu\text{m}$  wavelength range is derived by extrapolation from the 50 to 200  $\mu\text{m}$  wavelength range (grey line).

mic extrapolation, the temperature for the characteristic layer where most of the photospheric flux is formed ( $T_{(\tau_\lambda=1)}$ ) for the full 200 to 7500  $\mu\text{m}$  wavelength range is determined (see Fig. 1). The continuum flux at each far-infrared wavelength point is then approximated by the blackbody flux at the characteristic temperature  $B_\lambda(T)$  scaled with the appropriate angular diameter. Since we are in the Rayleigh-Jeans part of the spectrum, the flux value is quite insensitive to the temperature, i.e.  $\partial B_\lambda(T)/\partial T$  is small.

The accuracy and resolution of today’s FIR instruments remain currently too poor to constrain the importance of line veiling in the (sub)millimeter range. The study by Decin & Eriksson (2007) and B. Plez in case of the 40 – 665  $\mu\text{m}$  spectrum for  $\alpha$  Tau (*priv. comm.*) shows that molecular line absorption at a resolution of  $\sim 1500$  is typically less than 1% beyond 150  $\mu\text{m}$ . We therefore will compare the (sub)millimeter observational data with *continuum* flux predictions.

The input parameters for the MARCS code were taken from Decin et al. (2003a) unless indicated otherwise in Table 6. In the same article a discussion about the uncertainties on these parameters can be found. The models were reddened according to the value of the interstellar extinction derived from the model of Arenou et al. (1992) using the distances from Decin et al. (2003a) or Ochsenbein & Halbwachs (1999). The values of the interstellar extinction and the distances are listed in Table 6.

Fig. 2 shows the photometric data in comparison with the MARCS models. For all targets, the theoretical predictions underestimate the observations in the millimeter and/or centimeter wavelength area. Where an excess is detectable at 1.2 mm, the model underestimates the observations by an average of 25%. At centimeter wavelengths, the discrepancy amounts to

an average of 90%. In the following section, different causes for this excess are explored.

## 5. Discussion

### 5.1. Proof for a significant flux excess at 1.2 mm

Fig. 2 shows clear indications for a flux excess at millimeter and centimeter wavelengths. To prove the flux excess, both the observational and theoretical uncertainties in the atmosphere models should first be investigated.

**Observational uncertainties** The uncertainties on the observations in the millimeter/centimeter wavelength region are typically of the order of 15%. The IRAS-PSC error bars given in the catalogue are the statistical  $1\sigma$  uncertainty values; realistic absolute calibration uncertainties are lacking for the PSC, but are estimated to be 20% (*D. Kester, priv. comm.*). This higher uncertainty was already clear from a comparison between the Infrared Space Observatory - Short Wavelength Spectrometer (ISO-SWS) data and the IRAS-PSC and IRAS-LRS data (Van Malderen et al. 2004). Therefore we have used an error bar of 20% on the IRAS-PSC data in our analysis. The IRAS-PSC fluxes are also colour corrected.

The uncertainties on the near- and mid infrared photometry were taken from the catalogs mentioned in Sect. 3.

**Theoretical uncertainties** As described in Decin & Eriksson (2007), the uncertainty on the FIR continuum flux predictions mainly arise from uncertainties on (1.) the estimated stellar temperature and (2.) the neglect of some physical processes.

(1.) In the FIR, the dominant continuous opacity arises from  $\text{H}^-$  free-free absorption, whose absorption coefficients are nowadays known at an accuracy of about 1% for wavelengths beyond 0.5  $\mu\text{m}$  over the temperature range between 1000 and 10000 K (Decin & Eriksson 2007). An uncertainty in the estimated stellar temperature may give rise to an uncertainty on the continuum predictions of up to 4% for A-M giants.

(2.) Since we are tracing regions high up in the atmosphere, density inhomogeneities and patchy temperature structures may occur. This kind of 3-dimensional structures are not dealt with in the 1-dimensional MARCS model atmosphere code. Luckily, the wavelength regions of interest are in the FIR, where the sensitivity of the Planck function to the temperature is small. Another important physical process not included in the MARCS atmosphere code is the presence of circumstellar dust and/or a chromosphere or ionized wind. While the latter is the topic of this study, the first excess can be excluded from the detailed analysis of the ISO-SWS data for 7 targets in our sample Decin et al. (2003a) and Van Malderen et al. (2004).  $\iota$  Aur and  $\sigma$  Lib were not observed by ISO, but good-quality IRAS-LRS data exist for both objects. The IRAS-LRS data show no sign of flux excess due to circumstellar dust.

A remark concerning the angular diameters that were used to compute the fundamental parameters for the MARCS models is in place here. The angular diameters are computed from

**Table 6.** Input parameters for the MARCS code from Decin et al. (2003a) unless indicated otherwise: the effective temperature  $T_{\text{eff}}$  in K, the gravity  $\log g$  in  $\text{cm/s}^2$ , the microturbulent velocity  $\xi_t$  in  $\text{km s}^{-1}$ , the metallicity  $[\text{Fe}/\text{H}]$ , the abundances of carbon, nitrogen, and oxygen, the  $^{12}\text{C}/^{13}\text{C}$ -ratio and the photospheric stellar angular diameter  $\theta_d$  in milliarcseconds. The calculation of the angular diameter is discussed in Sect. 5.1. The table also contains the distances (in pc) and the values of the interstellar extinction  $A_v$  as derived from the model of Arenou et al. (1992). Values, for which no literature values have been found, have been assumed on the basis of analogue objects, and are listed in italics.

	$\alpha$ Boo	$\iota$ Aur	$\beta$ UMi	$\gamma$ Dra	$\alpha$ Tau
Sp. Type	K2 IIIp	K3 II	K4 III	K5 III	K5 III
$T_{\text{eff}}$	$4320 \pm 140$	$4160 \pm 130^1$	$4085 \pm 140$	$3960 \pm 140$	$3850 \pm 140$
$\log g$	$1.5 \pm 0.15$	$1.74 \pm 0.36^1$	$1.6 \pm 0.02$	$1.30 \pm 0.25$	$1.50 \pm 0.15$
$\xi_t$	$1.7 \pm 0.5$	$3.00 \pm 0.5^1$	$2 \pm 0.5$	$2.0 \pm 0.5$	$1.7 \pm 0.5$
$[\text{Fe}/\text{H}]$	$-0.50 \pm 0.20$	$-0.11 \pm 0.22^1$	$-0.15 \pm 0.2$	$0.00 \pm 0.20$	$-0.15 \pm 0.20$
$\epsilon(\text{C})$	$7.96 \pm 0.20$	8.35	$8.25 \pm 0.2$	$8.15 \pm 0.25$	$8.35 \pm 0.20$
$\epsilon(\text{N})$	$7.61 \pm 0.25$	8.35	$8.16 \pm 0.25$	$8.26 \pm 0.25$	$8.35 \pm 0.25$
$\epsilon(\text{O})$	$8.68 \pm 0.20$	8.93	$8.83 \pm 0.2$	$8.93 \pm 0.20$	$8.93 \pm 0.20$
$^{12}\text{C}/^{13}\text{C}$	$7 \pm 2$	10	$9 \pm 2$	$10 \pm 2$	$10 \pm 2$
$\theta_d$	$20.74 \pm 0.10$	$7.05 \pm 0.03$	$9.03 \pm 0.42$	$9.94 \pm 0.05$	$20.89 \pm 0.10$
distance	$11.26 \pm 0.09$	$166.56 \pm 33.31^5$	$39.87 \pm 7.97^5$	$45.25 \pm 0.94$	$19.96 \pm 0.38$
$M_g$	$0.73 \pm 0.27$	3.6	$2.49 \pm 0.92$	$1.72 \pm 1.02$	$2.30 \pm 0.85$
$A_v$	$0.01 \pm 0.15$	$0.00 \pm 0.15$	$0.00 \pm 0.5$	$0.03 \pm 0.15$	$0.03 \pm 0.15$
	$\beta$ And	$\alpha$ Cet	$\beta$ Peg	$\sigma$ Lib	
Sp. Type	M0 III	M2 III	M2.5 III	M3/M4 III	
$T_{\text{eff}}$	$3880 \pm 140$	$3740 \pm 140$	$3600 \pm 300$	$3634 \pm 110^2$	
$\log g$	$0.95 \pm 0.25$	$0.95 \pm 0.25$	$0.65 \pm 0.40$	$0.9 \pm 0.31^2$	
$\xi_t$	$2.0 \pm 0.5$	$2.3 \pm 0.5$	$2.0 \pm 0.3$	$3.1 \pm 0.5^3$	
$[\text{Fe}/\text{H}]$	$0.00 \pm 0.30$	$0.00 \pm 0.30$	0.00	0.00	
$\epsilon(\text{C})$	$8.12 \pm 0.30$	$8.20 \pm 0.30$	$8.20 \pm 0.40$	$8.23 \pm 0.04^3$	
$\epsilon(\text{N})$	$8.37 \pm 0.40$	$8.26 \pm 0.40$	$8.18 \pm 0.40$	$8.15 \pm 0.05^4$	
$\epsilon(\text{O})$	$9.08 \pm 0.30$	$8.93 \pm 0.30$	$8.93 \pm 0.40$	8.93	
$^{12}\text{C}/^{13}\text{C}$	$9 \pm 2$	$10 \pm 2$	$5 \pm 3$	10	
$\theta_d$	$13.03 \pm 0.06$	$12.34 \pm 0.06$	$16.43 \pm 0.08$	$11.00 \pm 0.05$	
distance	$61.12 \pm 2.84$	$67.48 \pm 3.78$	$61.08 \pm 2.69$	$90.80 \pm 18.16^5$	
$M_g$	$2.49 \pm 1.48$	$2.69 \pm 1.61$	$1.94_{-1.34}^{+4.27}$	1.5	
$A_v$	$0.06 \pm 0.15$	$0.06 \pm 0.16$	$0.03 \pm 0.15$	$0.20 \pm 0.17$	

<sup>1</sup> McWilliam (1990), <sup>2</sup> Judge & Stencel (1991), <sup>3</sup> Tsuji (1991), <sup>4</sup> Aoki & Tsuji (1997), <sup>5</sup> Ochsenbein & Halbwachs (1999)

Selby or TCS K-band photometry. For  $\beta$  Umi, we have used the Johnson K-band magnitude of  $-1.22$  (Faucherre et al. 1983), yielding a magnitude of  $-1.276$  in the Selby system. Zeropoints are calculated using the Kurucz theoretical spectrum of Vega, taking into account the observed near-IR excess of Vega (Absil et al. 2006). For the Selby photometric system we obtain a zeropoint of  $4.0517 \cdot 10^{-10} \text{ W/m}^2/\mu\text{m}$ , for TCS  $4.4506 \cdot 10^{-10} \text{ W/m}^2/\mu\text{m}$ . An uncertainty of 0.01 mag in the K-band photometric data (0.1 mag for  $\beta$  Umi) is propagated in the computation of the uncertainty on the angular diameter. At every wavelength, the observed angular diameter represents the apparent diameter of the stellar surface where  $\tau_\lambda \sim 1$ . Since at the longer wavelengths, we are tracing layers that lie further and further outwards, it is expected that the angular diameter increases with increasing wavelength. If the angular diameter in the millimeter and centimeter area is considerably larger than the assumed value, the MARCS models will underestimate the flux in this wavelength area.

To investigate this, we derived the change in height of the continuum forming layers with increasing wavelength for the M0 giant  $\beta$  And. The layer where  $\tau_{\text{ross}} = 1$  (with  $\tau_{\text{ross}}$  the Rosseland optical depth) defines the stellar radius, being in case of  $\beta$  And  $R_* = 6.12 \cdot 10^{12} \text{ cm}$ . The flux at  $100 \mu\text{m}$  is formed at  $R_* + 6.90 \cdot 10^{10} \text{ cm}$ , for  $150 \mu\text{m}$  at  $R_* + 7.89 \cdot 10^{10} \text{ cm}$  and for  $200 \mu\text{m}$  at  $R_* + 1.70 \cdot 10^{11} \text{ cm}$ . From the MARCS model we derive that the flux at  $7 \text{ cm}$  (this is the longest wavelength for which we have observations) is formed at  $R_* + 2.23 \cdot 10^{11} \text{ cm}$ , which corresponds to an increase in radius of 3.64%. For the other sample stars, comparable numbers are found. This increase in angular diameter is insufficient to explain the observed excess.

In general, the uncertainties on the theoretical flux predictions are in the order of 5 to 10%, excluding the effects of a chromosphere or ionized wind. The observed flux excesses are hence not caused by inaccuracies in the modeling, but are due to physical processes in the stars.

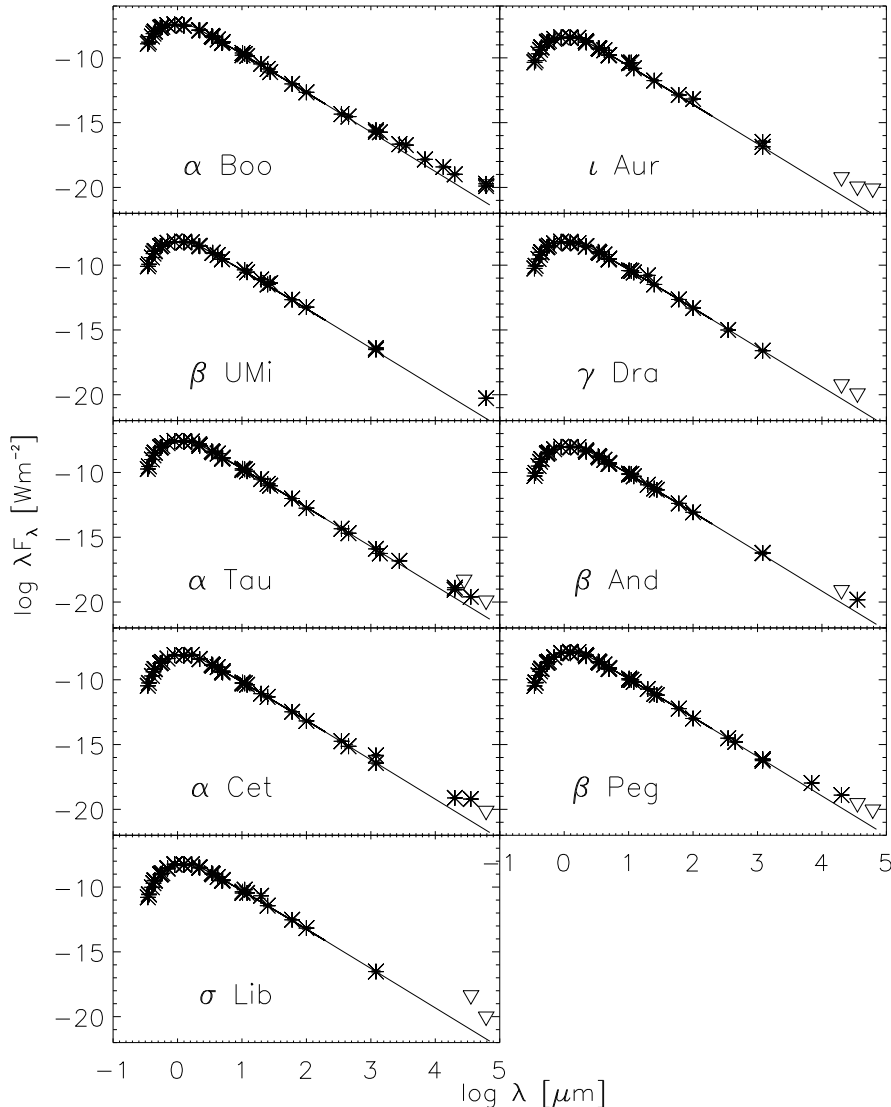


**Figure 2.** Comparison between the photometric data (asterisks) and the continuum theoretical MARCS spectrum (full line) for the nine sample stars. If several observations are available at the same wavelength, only the maximum and minimum flux value were plotted, except at (sub)millimeter and centimeter wavelengths as this wavelength region is of particular interest here. Most of the error bars fall within the symbols for the data. A reversed triangle represents an upper limit.

## 5.2. Brightness temperature

Fig. 3 provides another window at studying the flux excess. It shows the brightness temperature over the full  $5 \mu\text{m}$  to  $7 \text{ cm}$  wavelength range. The brightness temperature is defined as the temperature of a black body that gives the same flux as the model atmosphere at the indicated wavelength, and can be written as (Cohen et al. 2005)

$$T_B(\lambda) = \frac{14387.75/\lambda}{\ln\left(1 + \frac{733.4090 \theta_D^2}{F_\nu(\lambda)\lambda^3}\right)}, \quad (1)$$

where  $F_\nu$  is the observed flux in Jy,  $\theta_D$  the angular diameter in milliarcseconds,  $\lambda$  the wavelength in  $\mu\text{m}$ , and  $T_B(\lambda)$  the brightness temperature in K.

For comparison also the brightness temperatures from the theoretical models are plotted in Fig. 3. The uncertainty on the data and on the angular diameter (see previous section) has been propagated to determine the error bars on the observational brightness temperatures. The differences between the theoretical brightness temperatures (as derived from the MARCS predictions) taking the angular diameter uncertainty

into account are indiscernible. The uncertainty on the effective temperature has the highest influence on the theoretical brightness temperature predictions. This is illustrated in case of  $\beta \text{ UMi}$  in Figs. 3 and 4. In the approximation for long wavelengths, the formula for the brightness temperature shows that  $T_B(\lambda) \propto 1/\theta_D^2$ . Since the angular diameters at long wavelengths might be underestimated when an extra component besides the photosphere is present, the brightness temperatures in Fig. 3 should be regarded as upper limits.

In Fig. 3 one can clearly see the wavelength region where the flux excess starts for each of the sample stars. For  $\beta \text{ UMi}$ , the observation at  $60 \mu\text{m}$  still agrees with the model within the error. Moreover, also the IRAS-LRS and ISO-SWS data of  $\beta \text{ UMi}$  agree with the model predictions (Van Malderen et al. 2004). The flux at  $100 \mu\text{m}$  is in excess of the model. The same holds for  $\iota \text{ Aur}$ . Note that the IRAS flux at  $100 \mu\text{m}$  for  $\iota \text{ Aur}$  is of lesser quality than the other IRAS points used in our analysis. But recently a weak IR flux excess at  $70 \mu\text{m}$  has been found in the Spitzer-MIPS data (Gordon et al. 2007), which confirms our finding that the excess starts somewhere between

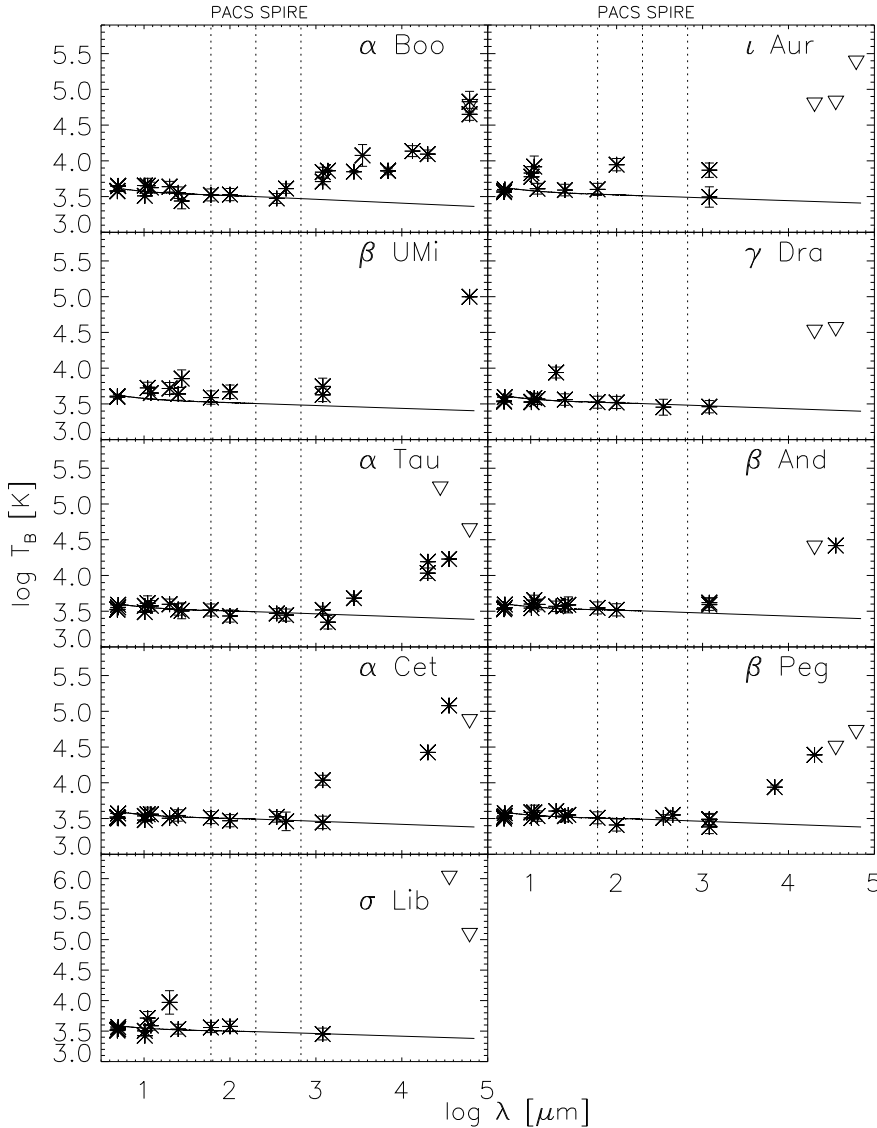


**Figure 3.** Brightness temperature  $T_B$  in function of the wavelength for the 9 sample stars between  $5 \mu\text{m}$  and  $7 \text{cm}$ . The full line indicates the brightness temperatures derived from the MARCS model, the asterisks show the brightness temperatures derived from the observations. A reversed triangle represents an upper limit. The error bars on the observational data take the uncertainty on the observations and on the angular diameter into account. The PACS and SPIRE wavelength ranges are indicated by a dotted line, to facilitate comparison to the wavelength region where a flux excess is seen. As an illustration of the influence of the effective temperature, three models with different  $T_{\text{eff}}$  are shown for  $\beta \text{UMi}$ . Fig. 4 gives a clearer view of these models.

$60 \mu\text{m}$  en  $100 \mu\text{m}$ . For  $\alpha \text{Boo}$ , the model and the data coincide for wavelengths up until  $350 \mu\text{m}$ . The measurement at  $450 \mu\text{m}$  lies above the model prediction and the data at longer wavelengths are all clearly in excess of the predictions. For  $\alpha \text{Cet}$  the excess seems to start between  $450 \mu\text{m}$  and  $1.2 \text{mm}$ , as the average flux at  $1.2 \text{mm}$  lies well above the model. For  $\beta \text{And}$  it starts between  $100 \mu\text{m}$  and  $1.2 \text{mm}$ ; unluckily no measurements are available between  $100 \mu\text{m}$  and  $1.2 \text{mm}$ . For  $\alpha \text{Tau}$  and  $\beta \text{Peg}$ , the excess starts at longer wavelengths, as the fluxes until  $1.38 \text{mm}$  (respectively  $1.2 \text{mm}$ ) are still in accordance with the predictions. For  $\gamma \text{Dra}$  and  $\sigma \text{Lib}$  all available data coincide with the model predictions, including the measurements at  $1.2 \text{mm}$ . However, there are no observational data at longer wavelengths and the upper limits at centimeter wavelengths are such that they do not exclude an excess.

It was already argued that the increase in angular diameter at longer wavelengths does not lead to significant changes in the MARCS predictions. However, possible extra components of the stellar atmosphere not taken into account by the MARCS-code, such as a chromosphere, can be extended in

volume in comparison to the stellar photosphere. Proof for this kind of extension can be found in for example Drake & Linsky (1986). They studied observations at  $2$  and  $6 \text{cm}$  of, a.o.,  $\alpha \text{Boo}$ . They treated the radiation at radio wavelengths as originating from an optically thick ionized wind (see also Sect. 5.5), for which they calculated the half-power radius (meaning that half of the radio emission originates from within this radius). For  $\alpha \text{Boo}$  this half-power radius at  $2 \text{cm}$  corresponds to the stellar radius, but at  $6 \text{cm}$  this radius had increased to  $\simeq 1.7 R_*$ . In the next sections, we will elaborate on the possibility that the flux excess arises from the presence of a chromosphere (corona) or from thermal emission in an ionized stellar wind.

### 5.3. Influence of a chromosphere at NIR wavelengths

In 1994, Wiedemann et al. studied the fundamental vibration-rotation lines of CO (at  $\sim 4.6 \mu\text{m}$ ) in a set of late-type stars. The CO  $\Delta v = 1$  lines are remote sensors for the thermal conditions in the outermost layers of the atmosphere. In particular,



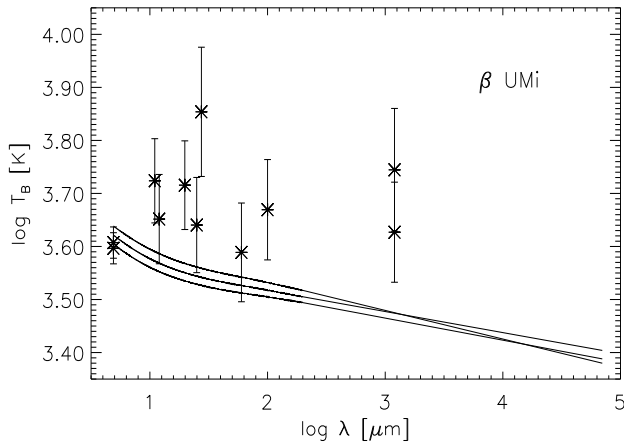


**Figure 4.** As an illustration of the influence of the effective temperature, three models with different  $T_{\text{eff}}$  are shown for  $\beta$  UMi. The effective temperature equals 3885, 4085 or 4285 K. A different scale than in Fig. 3 is used to enhance the region where the models differ. The observation at 6.14 cm is no longer visible here.

the strongest CO  $\Delta v = 1$  lines occur at or above the temperature minimum in chromospheric solar and stellar models. Wiedemann et al. (1994) found observational evidence in favor of a ‘thermal bifurcation’ model for the atmospheres of their sample stars. It consists of two distinct physical phases that coexist at chromospheric altitudes. One component is controlled by molecular cooling and is represented by a radiative equilibrium model atmosphere with CO induced temperature depression. The second component is chromospheric and features a temperature inversion produced by the deposition of mechanical energy. Any observed spectrum from an atmosphere with thermal bifurcation is to be interpreted as a spatial sum over the two types of thermal regions with appropriate geometrical weighting factors.

Wiedemann et al. (1994) concluded that the observed infrared CO  $\Delta v = 1$  spectrum at  $4.6 \mu\text{m}$  of one group of stars, containing  $\alpha$  Boo,  $\alpha$  Tau and  $\gamma$  Dra, is well described by homogeneous radiative equilibrium models. The near-IR CO spectra for this group of so-called ‘quiet’ stars indicate that the cool regions dominate the stellar surface for heights between  $\sim 10^{-1/2}$  and  $10^{-2}$  g/cm<sup>2</sup> in mass column density, and have large filling factors. These stars are said to have a ‘COMosphere’. For a second group of stars, the CO  $\Delta v = 1$  spectrum is poorly represented by radiative equilibrium models, and is compatible with a chromosphere covering the stellar surface homogeneously at these altitudes. After investigation of different chromospheric indicators, it also became clear that the stars in the first group show only little chromospheric activity.

Three stars from our sample,  $\alpha$  Boo,  $\alpha$  Tau and  $\gamma$  Dra, belong to the first group of ‘quiet stars’ i.e. their CO  $\Delta v = 1$  spectrum indicates that the COMosphere dominates the thermal structure at heights between  $\sim 10^{-1/2}$  and  $10^{-2}$  g/cm<sup>2</sup> in mass column density. For these stars, the spectrum at NIR wavelengths is not influenced by their chromospheric activity.

In the following sections, we investigate if this remains true at longer wavelengths.

#### 5.4. Coronal, transition region and wind dividing lines

Linsky & Haisch (1979) introduced a dividing line (further denoted by DL) in the cool part of the HR diagram on the basis of ultra-violet spectra of late-type stars. Stars to the blue side of the ‘transition region DL’ were termed ‘solar-type’, as they showed spectral lines formed at temperatures of  $5 \times 10^3 - 2 \times 10^5$  K, indicative of chromospheres, transition regions and by implication unseen coronae at even hotter temperatures. Stars to the red side are of ‘non-solar type’: they only exhibited lines formed at temperatures below 10 000 – 20 000 K, indicative of chromospheres only. Ayres et al. (1981) attempted to observe soft X-ray emission from late-type stars, being a signature of stellar coronae ( $T > 10^6$  K). They found an ‘X-ray DL’ roughly coinciding with the ‘transition region DL’ from Linsky & Haisch (1979); only stars to the blue side were detected in X-rays. Stencel & Mullan (1980) studied the morphology of Mg II h and k resonance lines and they also found a similar distinction in position in the HR-diagram between stars with a low-velocity wind in their chromosphere (to the red side of the line) and stars without (to the blue side).

Since the first discovery of the DLs, several authors have confirmed the dichotomy in late-type giant atmospheres, but more sensitive observations have also revised the location of the different DLs in the HR diagram. Hünsch et al. (1996) place the ‘X-ray DL’ at  $B - V = 1.2$  for luminosity class III giants. According to Reimers et al. (1996), the ‘wind DL’ runs vertically at  $B - V \approx 1.45$ , for  $B - V < 1.45$  it runs nearly horizontal to  $B - V \approx 1.0$  at  $M_{\text{bol}} \approx -2.8$ . And Haisch et al. (1990) found that the latest occurrence of emission lines from C IV or Si IV, indicative of a transition region, occurs at K4 III, corresponding to  $B - V = 1.385$  (Gray 1992). This places all of our eight stars with luminosity class III in the category of late-type stars with a chromosphere and a cool wind (see Table 1 and Fig. 5).  $\alpha$  Boo, although located to the blue side of the wind DL, is known to possess a cool wind (Ayres et al. 1982) and is regarded as an archetype of a non-coronal star. The K2 II giant  $\iota$  Aur was detected in X-rays by Reimers et al. (1996) and shows C IV and Si IV emission (Haisch et al. 1990), but also circumstellar Ca II H+K lines (Reimers et al. 1996). It is a so-called ‘hybrid’ giant. Hybrid giants are located to the red (i.e. non-coronal side) of the ‘transition region DL’, but show the existence of both transition region plasma and large mass-loss rates ( $10^{-9} - 10^{-10} M_{\odot}/\text{yr}$ ) (Harper 1992).

It should, however, be noted that the distinction between coronal and non-coronal giants is not so clear-cut. In a number of recent articles, evidence is given that all giants show some level of X-ray emission when observed with sufficient sensitivity. On the other hand, all observations confirm the significant drop in X-ray emission around early K spectral type for luminosity class III.

X-ray emission from cool stars is linked to the confinement of hot coronal matter in magnetic structures. An under-

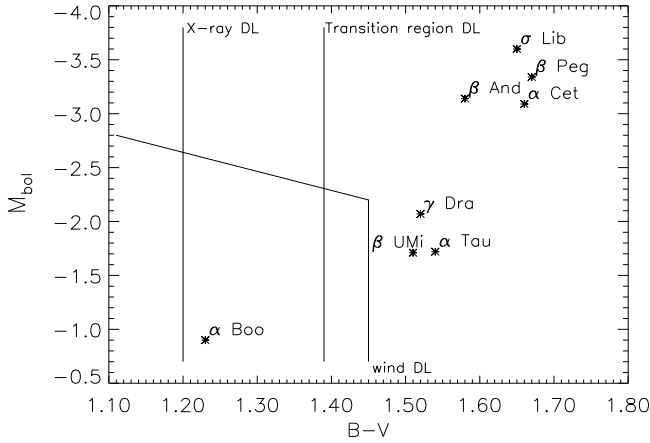


**Figure 5.** The position of the different DLs in the HR diagram, together with the eight luminosity class III giants from our sample. The ‘X-ray DL’ is derived by Hünsch et al. (1996), the ‘transition region DL’ by Haisch et al. (1990), and the ‘wind DL’ by Reimers et al. (1996) (see text for more details).

standing of the origin of these magnetic structures is closely related to the physical explanation for the existence of the DLs, both of which are still under discussion. Most authors seem to agree on the fact that a change in surface magnetic field topology is responsible for the existence of the DLs. According to Rosner et al. (1995), the field topology of a red giant changes from a large scale organized and closed configuration binding coronal gas, to a largely open magnetic field giving rise to a massive cool wind, as the star evolves along the RGB from the left of the DLs to the right. The transition in topology is ascribed to a change in the origin of the field: as the stellar rotation drops below a critical value, the spin-catalyzed dynamo gives way to a field generation mechanism requiring fluid turbulence as found in the convection zone. It has also been suggested that the magnetic flux tubes that rise up from underneath the convection zone to the stellar surface where they form large scale coronal loops, become trapped in the convective envelope as the convection zone deepens to the right of the DLs (Holzwarth & Schüssler 2001). However, Ayres et al. (1997, 2003) have found evidence in “non-coronal” giants that coronal loops can still rise to the stellar surface: the loops extend beyond the cold molecular layer just above the stellar photosphere, but are at least partially submerged in the chromosphere/COMosphere, where the coronal X-rays are attenuated by overlying material. It is also still unclear if stars evolving along the RGB cross the DLs (as was a.o. postulated by Rosner et al. 1995), or if the evolution tracks run parallel to them (Hünsch et al. 1996). In this last scenario, the difference in X-ray activity on either side of the DLs would be due to a different rotational history of each star implying a difference in spin-catalyzed dynamo strength.

In the following sections we will investigate if the observed flux excess in the (sub)millimeter and centimeter wavelength range in our selected late-type giants can be explained by the presence of a chromosphere (corona) and/or by thermal emis-

sion from an ionized stellar wind. As we shall show in Sect. 5.5 and Sect. 5.6, the radiation coming from a chromosphere or from an ionized wind exhibits a different frequency dependence  $F_\nu \propto \nu^\alpha$ . The spectral indices  $\alpha$  as determined from the available observations will be compared to the theoretical predictions to determine the cause of the flux excess.

### 5.5. Thermal emission from an ionized wind

Stars with an ionized wind emit an excess of continuum emission at long wavelengths, i.e. from the IR to the radio region, in addition to the black body flux emission. This excess flux is due to free-free emission or Bremsstrahlung from the wind. To derive the wavelength dependence of the thermal emission from an ionized wind, we will use a model from Olzon (1975). This article gives analytic expressions for the flux originating from a stellar wind, assuming a homogeneous, spherical geometry with a uniform electron temperature and with H II as the only constituent. In reality, the hydrogen in the winds of these late-type stars will be only partially ionized (Drake et al. 1987). The free-free absorption coefficient per unit mass  $\kappa_\nu^{ff}$  in  $\text{cm}^2 \text{g}^{-1}$  of an ionized gas at long wavelengths is (e.g. Lamers & Cassinelli 1999)

$$\kappa_\nu^{ff} = 1.78 \cdot 10^{-2} Z^2 \nu^{-2} g_\nu T^{-3/2} \frac{n_i n_e}{\rho} \quad (2)$$

where  $Z^2$  is the square of the charge of the atoms,  $n_e$  and  $n_i$  are the electron and ion densities in  $\text{cm}^{-3}$ ,  $\rho$  is the density in  $\text{g cm}^{-3}$  and  $g_\nu$  is the gaunt factor which will be approximated by a power law

$$g_\nu \simeq 1.37 T^{0.135} \lambda^{0.084} \quad (3)$$

where  $\lambda$  is expressed in cm. It is clear from these expressions that the wavelength dependence of the emitted flux will be the same, regardless of the main contributor to the flux, be it H<sup>-</sup> ff or H I ff.

Model V from Olzon (1975), the truncated power law distribution is of particular interest here. It assumes an electron density distribution with a homogeneous sphere in its centre:  $n_e \propto r^{-2}$  for  $r \geq R$ , for  $r \leq R$   $n_e$  is constant. Using Eq. (2) in his expressions, the model predicts  $F_\nu \propto \nu^{0.611}$  in the optically thick limit and  $F_\nu \propto \nu^{-0.084}$  in the optically thin limit. These approximations can be generalised to density distributions  $n_e \propto r^{-\beta}$  with  $\beta > 1.5$ . A value for  $\beta$  differing from 2 can be caused by a non-constant velocity distribution in the wind. This is a very plausible explanation if the radio emission originates from the wind acceleration zone. A decreasing (increasing) fractional ionisation rate (this is the number of free electrons per neutral hydrogen atom) with radius can also lead to a higher (lower) value for  $\beta$ . An extreme case of this scenario would be the existence of an outer cutoff radius  $r_0$  to the ionized portion of the wind. Although doubtful for the targets in our study, this cutoff might be caused for example by the formation of dust at this location in the wind, ‘quenched’ the ionized material (Drake & Linsky 1986). The spectral index would change for  $\nu < \nu_0$ , where  $\nu_0$  is determined by the cutoff radius. For K to mid M cool wind giants, most estimates of the dust-formation region (if present at all) indicate  $r_0/R_* \approx 10$ .

It can be shown that the spectrum is only influenced by this transition for  $\lambda \gtrsim 30$  cm (Drake & Linsky 1986). No observations beyond this wavelength are being used in this article, hence such a spatial restriction of the ionized region is of no importance for our discussion.

In the optically thin case the wavelength dependence is not influenced by the value for  $\beta$ . In the optically thick case we have

$$F_\nu \propto \nu^\alpha \quad \text{with} \quad \alpha = \frac{2\beta - 3.084}{\beta - 0.5}. \quad (4)$$

For  $\beta = 1.5$  we find  $\alpha = -0.084$ , which is the same frequency dependence as in the optically thin case.  $\alpha$  goes asymptotically to 2 as  $\beta \rightarrow +\infty$ , but we do expect  $\beta$  to fluctuate around 2.

### 5.6. Chromospheric emission

The continuum radiation from a chromosphere will be mainly free-free emission from  $H^-$  and  $H I$ . The flux can be written as

$$F_\lambda = \kappa_\lambda^{ff} \rho B_\lambda(T) V \quad (5)$$

in the optically thin case, where  $V$  is the volume of the emitting region and  $B_\lambda$  is the Planck function. This expression can be derived from Eq. (1) in Olon (1975), see also Skinner & Whitmore (1987). With the use of Eq. (2) and the Rayleigh-Jeans approximation for the Planck function where  $B_\lambda(T) \propto \lambda^{-4}$ , we find a wavelength dependence of  $F_\lambda \propto \lambda^{-1.916}$ . In case of an optically thick chromosphere, we are looking at a black body with a temperature equal to the electron temperature at the layer where  $\tau_\lambda = 1$ . In that case we find  $F_\lambda \propto \lambda^{-4}$ . In the above approximations, the chromosphere is treated as a homogeneous region, with uniform densities and electron temperature.

The model above is also applicable to thermal emission from a corona. This implies that the same wavelength dependence will be found for corona and chromosphere and that our analysis will not allow to discriminate between these two sources of free-free emission.

### 5.7. Spectral indices for our program stars

Fig. 6 shows the true flux excess (the theoretically calculated flux is already subtracted from the data) at millimeter/centimeter wavelengths. We have chosen to plot  $\lambda^4 F_\lambda$  in function of wavelength on a logarithmic scale, since the data then follow a horizontal line in case of an optically thick chromosphere. To determine the spectral indices, we searched for the best fitting line through our data using a least-squares method. The starting point for these lines coincides with the first wavelength where a flux excess is noticeable (see Sect. 5.2), except for  $\iota$  Aur (see later in this section). For the least-squares fit we did not take any upper limits into account. Table 7 summarizes which spectral indices are expected for a chromosphere and for an ionized wind based on the simplified analytic expressions derived above.

The least-squares fits for  $\alpha$  Cet and  $\beta$  Peg have slopes of 1.2. This value lies closest to the spectral index expected for an

	optically thin	optically thick
chromosphere	$\lambda^4 F_\lambda \propto \lambda^{2.1}$	$\lambda^4 F_\lambda \propto \lambda^0$
ionized wind	$\lambda^4 F_\lambda \propto \lambda^{2.1}$	$\lambda^4 F_\lambda \propto \lambda^{1.4}$

**Table 7.** Summary of the wavelength dependencies of the flux derived for simplified models for the chromosphere and the ionized wind. The table gives the wavelength dependence for an optically thick ionized wind with a density distribution  $n_e \propto r^{-\beta}$  with  $\beta = 2$ . For  $\beta = 1.5$  we have  $\lambda^4 F_\lambda \propto \lambda^{2.1}$  and for  $\beta \rightarrow \infty$  we have  $\lambda^4 F_\lambda \propto \lambda^0$ .

optically thick ionized wind, with  $\beta$  equal to 2.2. For  $\beta$  And,  $\alpha$  Tau,  $\beta$  UMi and  $\alpha$  Boo, the slopes have values of respectively 0.9, 0.8, 0.7 and 0.7. These values lie somewhere in between the slope of an optically thick ionized wind (with  $\beta$  equal to respectively 2.8, 3.1, 3.5 and 3.5) and an optically thick chromosphere. For  $\iota$  Aur only two fluxes are available in excess of the model, among which the IRAS flux at  $100 \mu\text{m}$  which is of lesser quality. A least-squares fit to these two points leads to a slope of  $-0.5$ . For a better determination of the slope, we can include the IRAS flux at  $60 \mu\text{m}$ , which is of normal quality and just barely agrees with the model within the error. This fit gives a slope of 0.1 (see Fig. 6). Hence, only for  $\iota$  Aur, an optically thick chromosphere is found.

For all stars except  $\iota$  Aur and  $\alpha$  Boo, the least-squares fits are made to data at wavelengths longer than 1.2 mm, because only from this wavelength onwards a flux excess was detectable. In these cases, an optically thick ionized wind is the most likely explanation for the observed excess, although the density distributions sometimes show quite large deviations from the average  $n_e \propto r^{-2}$ . The only star where an optically thick chromosphere is seen, the hybrid giant  $\iota$  Aur, has a line fitted only to wavelengths shorter than 1.2 mm, because the flux excess was already present in this region and no measurements at longer wavelengths were available. We therefore propose that at shorter wavelengths ( $\lambda \lesssim 1$  mm) an optically thick chromosphere is being sampled and at longer wavelengths the continuum forming layers lie further outwards in the atmosphere and the observations show an optically thick ionized wind. It is very well possible that for wavelengths slightly longer than  $\sim 1$  mm, the optically thick chromosphere is still visible, as this would explain the deviating values for  $\beta$  in the optically thick ionized winds.

## 6. Conclusions

In 7 out of the 9 K- and M-giants examined, a clear flux excess at millimeter and/or centimeter wavelengths was found, for the other two targets only observational upper limits are available at centimeter wavelengths. The selected stars have low chromospheric and coronal activity and three of them do belong to the group of so-called ‘quiet’ K- and M-giants, where the near-infrared CO  $\Delta v = 1$  lines indicate that the CO-cooled regions, as predicted by radiative equilibrium models, dominate over the chromosphere at altitudes between  $\sim 10^{-1/2}$  and  $10^{-2}$  g/cm<sup>2</sup> in mass column density. On the basis of this study, it seems

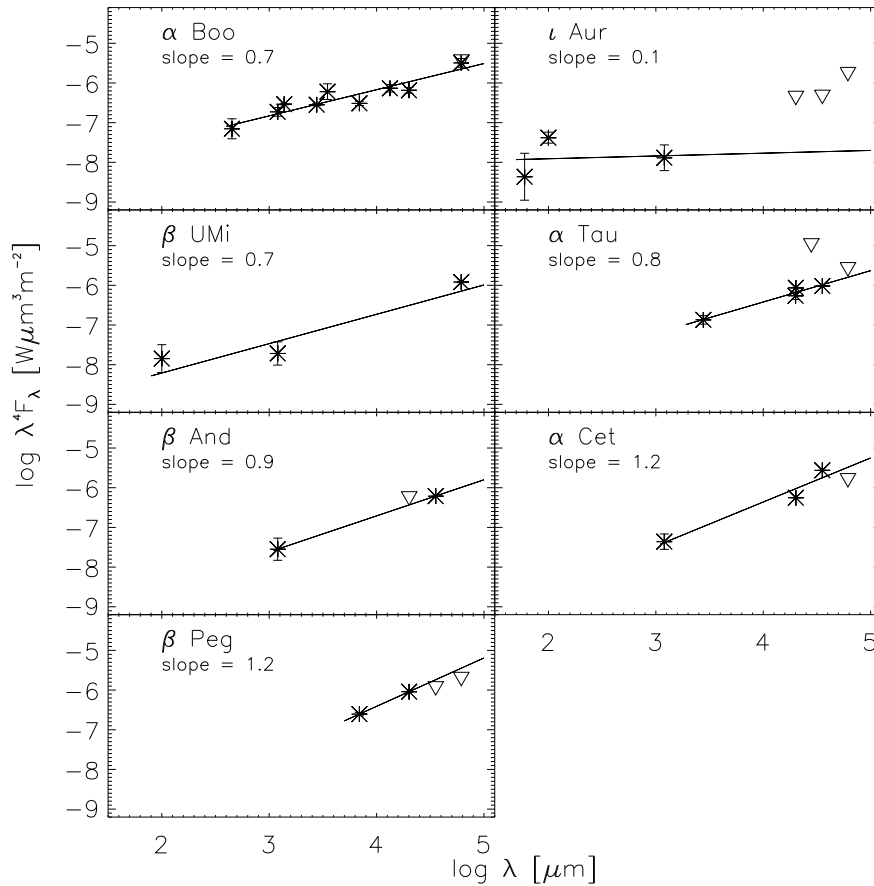


**Figure 6.** These figures show the true flux excess for the 7 stars in our sample for which a clear flux excess is detected (i.e.  $\gamma$  Dra and  $\sigma$  Lib are excluded, since only upper limits are available). The observations (with the continuum already subtracted) are represented by asterisks. The full lines show the linear least-squares fit to the data. If there were different measurements at one wavelength, the fluxes were replaced by a weighted average. Error bars are shown, but they often fall within the symbols for the fluxes. A triangle represents an upper limit. The slope for each target is indicated in the upper corner of each panel.

that for these stars the homogeneous atmosphere models based on radiative equilibrium are able to reproduce the CO spectrum around  $4.6 \mu\text{m}$ , but clearly fail to reproduce the flux at millimeter and centimeter wavelengths. At these far-IR wavelengths, the presence of a chromosphere and ionized stellar wind cause a clear flux excess.

The observed excess at wavelengths shorter than  $\sim 1 \text{ mm}$  is most likely to be attributed to an optically thick chromosphere, where an optically thick ionized wind is being sampled at longer wavelengths. The wavelength region where the excess starts depends upon the star under consideration. The most extreme cases are  $\iota$  Aur and  $\beta$  UMi, where the excess starts somewhere between  $60 \mu\text{m}$  and  $100 \mu\text{m}$ . These findings have implications for the roles of these standard stars as fiducial calibrators for PACS (wavelengths between  $60$  and  $210 \mu\text{m}$ ) and SPIRE (between  $200$  and  $670 \mu\text{m}$ ). For  $\alpha$  Boo the flux excess is already present at the SPIRE (but not at the PACS) wavelengths. For  $\alpha$  Cet it might be present at SPIRE wavelengths and for  $\beta$  And the excess might already start at the PACS wavelengths, but a lack of observations in these regions makes it impossible to indicate the precise start of the excess.  $\alpha$  Tau,  $\beta$  Peg,  $\gamma$  Dra and  $\sigma$  Lib show no flux excess in the PACS and SPIRE range, but especially for  $\sigma$  Lib, only few observations are available in the relevant region.  $\iota$  Aur and  $\beta$  UMi show a clear flux excess from  $100 \mu\text{m}$  onward, and should not be used as a calibrator beyond  $60 \mu\text{m}$ .

*Acknowledgements.* This work is based on observations collected at the European Southern Observatory, La Silla, Chile within program ESO 71.D-0600 and on observations collected with the IRAM 30m telescope within project 038\_03. We would like to thank R. Zylka and S. Leon for their support for the data reduction. The research at the Caltech Submillimeter Observatory is supported by grant AST-0540882 from the National Science Foundation.

SD and LD acknowledge financial support from the Fund for Scientific Research - Flanders (Belgium).

## References

- Aoki, W. & Tsuji, T. 1997, *A&A*, 328, 175  
 Arenou, F., Grenon, M., & Gomez, A. 1992, *A&A*, 258, 104  
 Ayres, T. R., Brown, A., & Harper, G. M. 2003, *ApJ*, 598, 610  
 Ayres, T. R., Brown, A., Harper, G. M., et al. 1997, *ApJ*, 491, 876  
 Ayres, T. R., Linsky, J. L., Vaiana, G. S., Golub, L., & Rosner, R. 1981, *ApJ*, 250, 293  
 Ayres, T. R., Simon, T., & Linsky, J. L. 1982, *ApJ*, 263, 791  
 Beichman, C. A., Neugebauer, G., Habing, H. J., Clegg, P. E., & Chester, T. J., eds. 1988, *Infrared astronomical satellite (IRAS) catalogs and atlases. Volume 1: Explanatory supplement, Vol. 1*  
 Cohen, M., Carbon, D., Welch, W., et al. 2005, *AJ*, 129, 2836  
 Decin, L. 2000, PhD thesis, Catholique University of Leuven Department of Physics and Astronomy

- Decin, L. & Eriksson, K. 2007, *A&A*, 472, 1041
- Decin, L., Morris, P. W., Appleton, P. N., et al. 2004, *ApJS*, 154, 408
- Decin, L., Vandebussche, B., Waelkens, C., et al. 2003a, *A&A*, 400, 709
- Decin, L., Vandebussche, B., Waelkens, C., et al. 2003b, *A&A*, 400, 679
- Decin, L., Vandebussche, B., Waelkens, C., et al. 2003c, *A&A*, 400, 695
- Dehaes, S., Groenewegen, M. A. T., Decin, L., et al. 2007, *MNRAS*, 377, 931
- Drake, S. A. & Linsky, J. L. 1986, *AJ*, 91, 602
- Drake, S. A., Linsky, J. L., & Elitzur, M. 1987, *AJ*, 94, 1280
- Ducati, J. R. 2002, *VizieR Online Data Catalog*, 2237, 0
- Eggen, O. J. & Stokes, N. R. 1970, *ApJ*, 161, 199
- Gordon, K. D., Engelbracht, C. W., Fadda, D., et al. 2007, *PASP*, 119, 1019
- Gray, D. F. 1992, *The Observation and Analysis of Stellar Photospheres (The Observation and Analysis of Stellar Photospheres, by David F. Gray, pp. 470. ISBN 0521408687. Cambridge, UK: Cambridge University Press, June 1992.)*
- Griffin, M. J. & Orton, G. S. 1993, *Icarus*, 105, 537
- Gustafsson, B., Bell, R. A., Eriksson, K., & Nordlund, A. 1975, *A&A*, 42, 407
- Haisch, B. M., Bookbinder, J. A., Maggio, A., Vaiana, G. S., & Bennett, J. O. 1990, *ApJ*, 361, 570
- Harper, G. M. 1992, *MNRAS*, 256, 37
- Holzwarth, V. & Schüssler, M. 2001, *A&A*, 377, 251
- Hünsch, M., Schmitt, J. H. M. M., Schroeder, K.-P., & Reimers, D. 1996, *A&A*, 310, 801
- Jenness, T., Stevens, J. A., Archibald, E. N., et al. 2002, *MNRAS*, 336, 14
- Judge, P. G. & Stencel, R. E. 1991, *ApJ*, 371, 357
- Kashyap, V., Rosner, R., Harnden, Jr., F. R., et al. 1994, *ApJ*, 431, 402
- Lamers, H. J. G. L. M. & Cassinelli, J. P. 1999, *Introduction to Stellar Winds (Cambridge University Press)*
- Linsky, J. L. & Haisch, B. M. 1979, *ApJ*, 229, L27
- McWilliam, A. 1990, *ApJS*, 74, 1075
- Morel, M. & Magnenat, P. 1978, *A&AS*, 34, 477
- Obrien, Jr., G. T. & Lambert, D. L. 1986, *ApJS*, 62, 899
- Ochsenbein, F. & Halbwegs, J. L. 1999, *VizieR Online Data Catalog*, 5053, 0
- Olnon, F. M. 1975, *A&A*, 39, 217
- Plez, B., Brett, J. M., & Nordlund, A. 1992, *A&A*, 256, 551
- Price, S. D. & Murdock, T. L. 1983, *NASA STI/Recon Technical Report N*, 84, 15005
- Reimers, D., Hünsch, M., Schmitt, J. H. M. M., & Toussaint, F. 1996, *A&A*, 310, 813
- Rosner, R., Musielak, Z. E., Cattaneo, F., Moore, R. L., & Suess, S. T. 1995, *ApJ*, 442, L25
- Rufener, F. 1989, *A&AS*, 78, 469
- Sandell, G. 1994, *MNRAS*, 271, 75
- Skinner, C. J. & Whitmore, B. 1987, *MNRAS*, 224, 335
- Skrutskie, M. F., Cutri, R. M., Stiening, R., et al. 2006, *AJ*, 131, 1163
- Smith, B., Price, S., & Baker, R. 2004, *ApJS*, 154, 673
- Stencel, R. E. & Mullan, D. J. 1980, *ApJ*, 238, 221
- Tsuji, T. 1991, *A&A*, 245, 203
- Van Malderen, R., Decin, L., Kester, D., et al. 2004, *A&A*, 414, 677
- Wendker, H. J. 1995, *A&AS*, 109, 177
- Wiedemann, G., Ayres, T. R., Jennings, D. E., & Saar, S. H. 1994, *ApJ*, 423, 806
- Wright, E. L. 1976, *ApJ*, 210, 250

# Online Material

## Appendix A: Summary of the photometric data used in this study

### List of Objects

' $\iota$  Aur' on page 2  
' $\sigma$  Lib' on page 2  
' $\alpha$  Boo' on page 2  
' $\beta$  And' on page 2  
' $\alpha$  Cet' on page 2  
' $\beta$  Peg' on page 2  
' $\alpha$  Boo' on page 2  
' $\iota$  Aur' on page 2  
' $\beta$  UMi' on page 2  
' $\gamma$  Dra' on page 2  
' $\alpha$  Tau' on page 2  
' $\beta$  And' on page 2  
' $\alpha$  Cet' on page 2  
' $\beta$  Peg' on page 2  
' $\sigma$  Lib' on page 2  
' $\alpha$  Tau' on page 3  
' $\alpha$  Boo' on page 3  
' $\alpha$  Cet' on page 3  
' $\beta$  Peg' on page 3  
' $\beta$  And' on page 3  
' $\alpha$  Boo' on page 3  
' $\alpha$  Cet' on page 3  
' $\alpha$  Cet' on page 3  
' $\alpha$  Boo' on page 3  
' $\alpha$  Boo' on page 3  
' $\alpha$  Cet' on page 3  
' $\beta$  Peg' on page 3  
' $\beta$  And' on page 3  
' $\beta$ ' on page 3  
' $\alpha$  Boo' on page 3  
' $\beta$  Peg' on page 3  
' $\alpha$  Boo' on page 3  
' $\alpha$  Boo' on page 3  
' $\beta$  Peg' on page 3  
' $\alpha$  Boo' on page 4  
' $\alpha$  Boo' on page 5  
' $\alpha$  Tau' on page 5  
' $\iota$  Aur' on page 5  
' $\sigma$  Lib' on page 5  
' $\beta$  Umi' on page 6  
' $\beta$  Umi' on page 6  
' $\beta$  And' on page 6  
' $\beta$  And' on page 6  
' $\beta$  UMi' on page 7  
' $\iota$  Aur' on page 7  
' $\iota$  Aur' on page 7  
' $\beta$  UMi' on page 8  
' $\alpha$  Boo' on page 8  
' $\alpha$  Cet' on page 8  
' $\beta$  And' on page 8  
' $\alpha$  Tau' on page 8  
' $\beta$  Peg' on page 8  
' $\gamma$  Dra' on page 8  
' $\sigma$  Lib' on page 8  
' $\alpha$  Boo' on page 8  
' $\alpha$  Boo' on page 8  
' $\beta$  UMi' on page 9  
' $\alpha$  Boo' on page 9  
' $\alpha$  Tau' on page 9  
' $\gamma$  Dra' on page 9  
' $\alpha$  Boo' on page 9  
' $\alpha$  Tau' on page 9  
' $\gamma$  Dra' on page 9  
' $\alpha$  Boo' on page 9  
' $\iota$  Aur' on page 9  
' $\iota$  Aur' on page 11  
' $\alpha$  Cet' on page 11  
' $\beta$  Peg' on page 11  
' $\beta$  And' on page 11  
' $\alpha$  Tau' on page 11  
' $\beta$  UMi' on page 11  
' $\alpha$  Boo' on page 11  
' $\iota$  Aur' on page 11  
' $\iota$  Aur' on page 11  
' $\iota$  Aur' on page 11  
' $\alpha$  Boo' on page 11  
' $\iota$  Aur' on page 11  
' $\gamma$  Dra' on page 12  
' $\sigma$  Lib' on page 12  
' $\iota$  Aur' on page 12  
' $\beta$  UMi' on page 12  
' $\alpha$  Boo' on page 12  
' $\alpha$  Cet' on page 12  
' $\beta$  And' on page 12  
' $\alpha$  Tau' on page 12  
' $\beta$  Peg' on page 12  
' $\gamma$  Dra' on page 12  
' $\sigma$  Lib' on page 12  
' $\sigma$  Lib' on page 12  
' $\iota$  Aur' on page 12  
' $\beta$  UMi' on page 12  
' $\alpha$  Boo' on page 3  
' $\iota$  Aur' on page 3  
' $\beta$  UMi' on page 4  
' $\gamma$  Dra' on page 4  
' $\alpha$  Tau' on page 5  
' $\beta$  And' on page 5  
' $\alpha$  Cet' on page 6  
' $\beta$  Peg' on page 6  
' $\sigma$  Lib' on page 7

**Table A.1.** Photometric data used in this study for the targets  $\alpha$  Boo and  $\iota$  Aur. The literature references are specified at the end of Table A.5.

$\alpha$ Boo			$\iota$ Aur		
$\lambda$ [ $\mu\text{m}$ ]	$\lambda F_\lambda$ [ $\text{Wm}^{-2}$ ]	ref.	$\lambda$ [ $\mu\text{m}$ ]	$\lambda F_\lambda$ [ $\text{Wm}^{-2}$ ]	ref.
$3.46 \cdot 10^{-1}$	$1.22 \cdot 10^{-9} \pm 1.77 \cdot 10^{-11}$	4	$3.46 \cdot 10^{-1}$	$4.49 \cdot 10^{-11} \pm 2.48 \cdot 10^{-13}$	4
$3.60 \cdot 10^{-1}$	$1.62 \cdot 10^{-9} \pm 0.00$	1	$3.60 \cdot 10^{-1}$	$6.23 \cdot 10^{-11} \pm 0.00$	1
$4.01 \cdot 10^{-1}$	$4.37 \cdot 10^{-9} \pm 6.35 \cdot 10^{-11}$	4	$4.01 \cdot 10^{-1}$	$2.05 \cdot 10^{-10} \pm 1.13 \cdot 10^{-12}$	4
$4.23 \cdot 10^{-1}$	$7.40 \cdot 10^{-9} \pm 9.27 \cdot 10^{-11}$	4	$4.23 \cdot 10^{-1}$	$4.12 \cdot 10^{-10} \pm 1.70 \cdot 10^{-12}$	4
$4.40 \cdot 10^{-1}$	$1.02 \cdot 10^{-8} \pm 0.00$	1	$4.40 \cdot 10^{-1}$	$6.20 \cdot 10^{-10} \pm 0.00$	1
$4.48 \cdot 10^{-1}$	$1.08 \cdot 10^{-8} \pm 1.57 \cdot 10^{-10}$	4	$4.48 \cdot 10^{-1}$	$6.48 \cdot 10^{-10} \pm 3.58 \cdot 10^{-12}$	4
$5.39 \cdot 10^{-1}$	$2.02 \cdot 10^{-8} \pm 2.93 \cdot 10^{-10}$	4	$5.39 \cdot 10^{-1}$	$1.55 \cdot 10^{-9} \pm 8.55 \cdot 10^{-12}$	4
$5.49 \cdot 10^{-1}$	$2.15 \cdot 10^{-8} \pm 2.18 \cdot 10^{-10}$	4	$5.49 \cdot 10^{-1}$	$1.69 \cdot 10^{-9} \pm 3.12 \cdot 10^{-12}$	4
$5.50 \cdot 10^{-1}$	$2.17 \cdot 10^{-8} \pm 0.00$	1	$5.50 \cdot 10^{-1}$	$1.74 \cdot 10^{-9} \pm 0.00 \cdot 10^{+00}$	1
$5.81 \cdot 10^{-1}$	$2.48 \cdot 10^{-8} \pm 3.60 \cdot 10^{-10}$	4	$5.81 \cdot 10^{-1}$	$2.02 \cdot 10^{-9} \pm 1.12 \cdot 10^{-11}$	4
$7.00 \cdot 10^{-1}$	$3.30 \cdot 10^{-8} \pm 0.00$	1	$7.00 \cdot 10^{-1}$	$2.88 \cdot 10^{-9} \pm 0.00$	1
$7.00 \cdot 10^{-1}$	$3.33 \cdot 10^{-8} \pm 0.00$	6	$9.00 \cdot 10^{-1}$	$3.84 \cdot 10^{-9} \pm 0.00$	1
$9.00 \cdot 10^{-1}$	$3.77 \cdot 10^{-8} \pm 0.00$	1	1.24	$3.98 \cdot 10^{-9} \pm 6.89 \cdot 10^{-10}$	12
$9.00 \cdot 10^{-1}$	$3.81 \cdot 10^{-8} \pm 0.00$	6	1.25	$3.31 \cdot 10^{-9} \pm 0.00$	1
1.24	$3.08 \cdot 10^{-8} \pm 4.45 \cdot 10^{-9}$	12	1.25	$3.40 \cdot 10^{-9} \pm 0.00$	6
1.25	$2.88 \cdot 10^{-8} \pm 0.00$	1	1.66	$3.51 \cdot 10^{-9} \pm 4.91 \cdot 10^{-10}$	12
1.25	$3.28 \cdot 10^{-8} \pm 0.00$	6	2.16	$2.01 \cdot 10^{-9} \pm 2.93 \cdot 10^{-10}$	12
2.16	$1.35 \cdot 10^{-8} \pm 2.11 \cdot 10^{-9}$	12	2.20	$1.53 \cdot 10^{-9} \pm 0.00$	1
2.20	$1.30 \cdot 10^{-8} \pm 0.00$	1	2.20	$1.60 \cdot 10^{-9} \pm 3.43 \cdot 10^{-11}$	7
2.20	$1.39 \cdot 10^{-8} \pm 1.53 \cdot 10^{-10}$	7	3.40	$5.65 \cdot 10^{-10} \pm 0.00$	1
3.40	$4.92 \cdot 10^{-9} \pm 0.00$	1	3.50	$5.30 \cdot 10^{-10} \pm 1.82 \cdot 10^{-11}$	7
3.40	$4.83 \cdot 10^{-9} \pm 0.00$	1	3.50	$4.83 \cdot 10^{-10} \pm 1.82 \cdot 10^{-11}$	7
3.50	$4.33 \cdot 10^{-9} \pm 1.03 \cdot 10^{-10}$	7	4.20	$3.80 \cdot 10^{-10} \pm 1.40 \cdot 10^{-10}$	2
3.50	$4.02 \cdot 10^{-9} \pm 1.03 \cdot 10^{-10}$	7	4.90	$1.62 \cdot 10^{-10} \pm 5.73 \cdot 10^{-12}$	7
4.20	$2.63 \cdot 10^{-9} \pm 7.26 \cdot 10^{-10}$	2	4.90	$1.53 \cdot 10^{-10} \pm 5.73 \cdot 10^{-12}$	7
4.90	$1.41 \cdot 10^{-9} \pm 1.56 \cdot 10^{-11}$	7	5.00	$1.65 \cdot 10^{-10} \pm 0.00$	1
4.90	$1.38 \cdot 10^{-9} \pm 1.56 \cdot 10^{-11}$	7	$1.02 \cdot 10^1$	$4.34 \cdot 10^{-11} \pm 0.00$	1
5.00	$1.65 \cdot 10^{-9} \pm 0.00$	1	$1.02 \cdot 10^1$	$3.81 \cdot 10^{-11} \pm 0.00$	6
5.00	$1.68 \cdot 10^{-9} \pm 0.00$	6	$1.10 \cdot 10^1$	$4.37 \cdot 10^{-11} \pm 1.61 \cdot 10^{-11}$	2
$1.02 \cdot 10^1$	$1.60 \cdot 10^{-10} \pm 0.00$	1	$1.20 \cdot 10^1$	$1.54 \cdot 10^{-11} \pm 3.07 \cdot 10^{-12}$	3
$1.02 \cdot 10^1$	$2.38 \cdot 10^{-10} \pm 0.00$	6	$2.50 \cdot 10^1$	$1.76 \cdot 10^{-12} \pm 3.53 \cdot 10^{-13}$	3
$1.10 \cdot 10^1$	$1.91 \cdot 10^{-10} \pm 5.27 \cdot 10^{-11}$	2	$6.00 \cdot 10^1$	$1.36 \cdot 10^{-13} \pm 2.73 \cdot 10^{-14}$	3
$1.20 \cdot 10^1$	$1.39 \cdot 10^{-10} \pm 2.79 \cdot 10^{-11}$	3	$1.00 \cdot 10^2$	$6.66 \cdot 10^{-14} \pm 1.33 \cdot 10^{-14}$	3
$1.98 \cdot 10^1$	$3.39 \cdot 10^{-11} \pm 6.25 \cdot 10^{-12}$	2	$1.20 \cdot 10^3$	$3.25 \cdot 10^{-17} \pm 7.50 \cdot 10^{-18}$	5
$2.50 \cdot 10^1$	$1.39 \cdot 10^{-11} \pm 2.78 \cdot 10^{-12}$	3	$1.20 \cdot 10^3$	$1.37 \cdot 10^{-17} \pm 4.50 \cdot 10^{-18}$	10
$2.74 \cdot 10^1$	$7.95 \cdot 10^{-12} \pm 2.20 \cdot 10^{-12}$	2	$2.01 \cdot 10^4$	$< 6.13 \cdot 10^{-20}$	5
$6.00 \cdot 10^1$	$9.79 \cdot 10^{-13} \pm 1.96 \cdot 10^{-13}$	3	$3.55 \cdot 10^4$	$< 1.18 \cdot 10^{-20}$	5
$1.00 \cdot 10^2$	$2.17 \cdot 10^{-13} \pm 4.35 \cdot 10^{-14}$	3	$6.14 \cdot 10^4$	$< 8.30 \cdot 10^{-18}$	5
$3.50 \cdot 10^2$	$4.53 \cdot 10^{-15} \pm 7.19 \cdot 10^{-16}$	13			
$4.50 \cdot 10^2$	$2.94 \cdot 10^{-15} \pm 4.46 \cdot 10^{-16}$	13			
$1.20 \cdot 10^3$	$2.64 \cdot 10^{-16} \pm 4.17 \cdot 10^{-17}$	9			
$1.20 \cdot 10^3$	$1.95 \cdot 10^{-16} \pm 2.00 \cdot 10^{-17}$	5			
$1.38 \cdot 10^3$	$1.82 \cdot 10^{-16} \pm 3.72 \cdot 10^{-18}$	8			
$2.77 \cdot 10^3$	$2.18 \cdot 10^{-17} \pm 7.48 \cdot 10^{-19}$	8			
$3.49 \cdot 10^3$	$1.84 \cdot 10^{-17} \pm 6.45 \cdot 10^{-18}$	5			
$6.92 \cdot 10^3$	$1.45 \cdot 10^{-18} \pm 8.23 \cdot 10^{-20}$	11			
$6.92 \cdot 10^3$	$1.43 \cdot 10^{-18} \pm 1.73 \cdot 10^{-19}$	11			
$1.33 \cdot 10^4$	$< 1.12 \cdot 10^{-17}$	5			
$1.33 \cdot 10^4$	$3.82 \cdot 10^{-19} \pm 6.74 \cdot 10^{-20}$	11			
$2.00 \cdot 10^4$	$1.02 \cdot 10^{-19} \pm 1.35 \cdot 10^{-20}$	5			
$2.80 \cdot 10^4$	$< 1.07 \cdot 10^{-18}$	5			
$6.14 \cdot 10^4$	$1.91 \cdot 10^{-20} \pm 6.35 \cdot 10^{-21}$	5			
$6.14 \cdot 10^4$	$1.27 \cdot 10^{-20} \pm 2.44 \cdot 10^{-21}$	5			
$6.17 \cdot 10^4$	$< 1.75 \cdot 10^{-20}$	5			



**Table A.2.** Photometric data used in this study for the targets  $\beta$  UMi and  $\gamma$  Dra. The literature references are specified at the end of Table A.5.

$\beta$ UMi			$\gamma$ Dra		
$\lambda$ [ $\mu\text{m}$ ]	$\lambda F_\lambda$ [ $\text{Wm}^{-2}$ ]	ref.	$\lambda$ [ $\mu\text{m}$ ]	$\lambda F_\lambda$ [ $\text{Wm}^{-2}$ ]	ref.
$3.46 \cdot 10^{-1}$	$8.12 \cdot 10^{-11} \pm 8.73 \cdot 10^{-13}$	4	$3.46 \cdot 10^{-1}$	$5.58 \cdot 10^{-11} \pm 4.45 \cdot 10^{-13}$	4
$3.60 \cdot 10^{-1}$	$1.17 \cdot 10^{-10} \pm 0.00$	1	$3.60 \cdot 10^{-1}$	$8.84 \cdot 10^{-11} \pm 0.00$	1
$4.01 \cdot 10^{-1}$	$3.91 \cdot 10^{-10} \pm 4.19 \cdot 10^{-12}$	4	$4.01 \cdot 10^{-1}$	$2.99 \cdot 10^{-10} \pm 2.38 \cdot 10^{-12}$	4
$4.23 \cdot 10^{-1}$	$7.79 \cdot 10^{-10} \pm 7.17 \cdot 10^{-12}$	4	$4.23 \cdot 10^{-1}$	$6.17 \cdot 10^{-10} \pm 4.02 \cdot 10^{-12}$	4
$4.40 \cdot 10^{-1}$	$1.15 \cdot 10^{-9} \pm 0.00$	1	$4.40 \cdot 10^{-1}$	$9.65 \cdot 10^{-10} \pm 0.00$	1
$4.48 \cdot 10^{-1}$	$1.24 \cdot 10^{-9} \pm 1.33 \cdot 10^{-11}$	4	$4.48 \cdot 10^{-1}$	$1.01 \cdot 10^{-9} \pm 8.04 \cdot 10^{-12}$	4
$5.39 \cdot 10^{-1}$	$2.78 \cdot 10^{-9} \pm 2.99 \cdot 10^{-11}$	4	$5.39 \cdot 10^{-1}$	$2.35 \cdot 10^{-9} \pm 1.88 \cdot 10^{-11}$	4
$5.49 \cdot 10^{-1}$	$3.01 \cdot 10^{-9} \pm 2.22 \cdot 10^{-11}$	4	$5.49 \cdot 10^{-1}$	$2.57 \cdot 10^{-9} \pm 1.18 \cdot 10^{-11}$	4
$5.50 \cdot 10^{-1}$	$3.06 \cdot 10^{-9} \pm 0.00$	1	$5.50 \cdot 10^{-1}$	$2.69 \cdot 10^{-9} \pm 0.00$	1
$5.81 \cdot 10^{-1}$	$3.66 \cdot 10^{-9} \pm 3.93 \cdot 10^{-11}$	4	$5.81 \cdot 10^{-1}$	$3.19 \cdot 10^{-9} \pm 2.54 \cdot 10^{-11}$	4
$7.00 \cdot 10^{-1}$	$5.28 \cdot 10^{-9} \pm 0.00$	1	$7.00 \cdot 10^{-1}$	$4.77 \cdot 10^{-9} \pm 0.00$	1
$9.00 \cdot 10^{-1}$	$6.68 \cdot 10^{-9} \pm 0.00$	1	$9.00 \cdot 10^{-1}$	$6.56 \cdot 10^{-9} \pm 0.00$	1
1.24	$6.10 \cdot 10^{-9} \pm 1.09 \cdot 10^{-09}$	12	1.24	$4.84 \cdot 10^{-9} \pm 9.46 \cdot 10^{-10}$	12
1.25	$6.43 \cdot 10^{-9} \pm 0.00$	6	1.25	$6.37 \cdot 10^{-9} \pm 0.00$	6
1.25	$5.64 \cdot 10^{-9} \pm 2.01 \cdot 10^{-10}$	7	1.25	$5.46 \cdot 10^{-9} \pm 2.20 \cdot 10^{-10}$	7
1.66	$5.82 \cdot 10^{-9} \pm 9.86 \cdot 10^{-10}$	12	1.66	$4.88 \cdot 10^{-9} \pm 8.09 \cdot 10^{-10}$	12
2.16	$3.03 \cdot 10^{-9} \pm 5.68 \cdot 10^{-10}$	12	2.16	$2.70 \cdot 10^{-9} \pm 3.97 \cdot 10^{-10}$	12
2.20	$3.09 \cdot 10^{-9} \pm 0.00$	6	2.20	$2.97 \cdot 10^{-9} \pm 0.00$	6
2.20	$2.85 \cdot 10^{-9} \pm 3.32 \cdot 10^{-11}$	7	2.20	$2.80 \cdot 10^{-9} \pm 4.24 \cdot 10^{-11}$	7
3.50	$9.18 \cdot 10^{-10} \pm 2.94 \cdot 10^{-11}$	7	3.40	$1.09 \cdot 10^{-9} \pm 0.00$	1
3.50	$8.69 \cdot 10^{-10} \pm 2.94 \cdot 10^{-11}$	7	3.40	$1.03 \cdot 10^{-9} \pm 0.00$	6
4.20	$6.02 \cdot 10^{-10} \pm 1.66 \cdot 10^{-10}$	2	3.50	$9.18 \cdot 10^{-10} \pm 2.45 \cdot 10^{-11}$	7
4.90	$2.92 \cdot 10^{-10} \pm 6.45 \cdot 10^{-12}$	7	3.50	$8.69 \cdot 10^{-10} \pm 2.45 \cdot 10^{-11}$	7
4.90	$2.82 \cdot 10^{-10} \pm 6.45 \cdot 10^{-12}$	7	4.20	$6.60 \cdot 10^{-10} \pm 1.82 \cdot 10^{-10}$	2
$1.10 \cdot 10^1$	$4.37 \cdot 10^{-11} \pm 8.05 \cdot 10^{-12}$	2	4.90	$2.84 \cdot 10^{-10} \pm 6.94 \cdot 10^{-12}$	7
$1.20 \cdot 10^1$	$2.82 \cdot 10^{-11} \pm 5.65 \cdot 10^{-12}$	3	4.90	$2.74 \cdot 10^{-10} \pm 6.94 \cdot 10^{-12}$	7
$1.98 \cdot 10^1$	$7.77 \cdot 10^{-12} \pm 1.43 \cdot 10^{-12}$	2	5.00	$3.23 \cdot 10^{-10} \pm 0.00$	6
$2.50 \cdot 10^1$	$3.26 \cdot 10^{-12} \pm 6.52 \cdot 10^{-13}$	3	$1.02 \cdot 10^1$	$3.81 \cdot 10^{-11} \pm 0.00$	1
$2.74 \cdot 10^1$	$4.17 \cdot 10^{-12} \pm 1.15 \cdot 10^{-12}$	2	$1.02 \cdot 10^1$	$3.88 \cdot 10^{-11} \pm 0.00$	1
$6.00 \cdot 10^1$	$2.17 \cdot 10^{-13} \pm 4.35 \cdot 10^{-14}$	3	$1.10 \cdot 10^1$	$3.63 \cdot 10^{-11} \pm 6.70 \cdot 10^{-12}$	2
$1.00 \cdot 10^2$	$5.73 \cdot 10^{-14} \pm 1.15 \cdot 10^{-14}$	3	$1.20 \cdot 10^1$	$2.72 \cdot 10^{-11} \pm 5.45 \cdot 10^{-12}$	3
$1.20 \cdot 10^3$	$4.00 \cdot 10^{-17} \pm 1.00 \cdot 10^{-17}$	5	$1.98 \cdot 10^1$	$1.62 \cdot 10^{-11} \pm 2.99 \cdot 10^{-12}$	2
$1.20 \cdot 10^3$	$3.05 \cdot 10^{-17} \pm 6.00 \cdot 10^{-18}$	10	$2.50 \cdot 10^1$	$3.24 \cdot 10^{-12} \pm 6.48 \cdot 10^{-13}$	3
$6.14 \cdot 10^4$	$5.37 \cdot 10^{-21} \pm 0.00$	5	$6.00 \cdot 10^1$	$2.25 \cdot 10^{-13} \pm 4.51 \cdot 10^{-14}$	3
			$1.00 \cdot 10^2$	$4.89 \cdot 10^{-14} \pm 9.77 \cdot 10^{-15}$	3
			$3.50 \cdot 10^2$	$9.94 \cdot 10^{-16} \pm 2.57 \cdot 10^{-16}$	3
			$1.20 \cdot 10^3$	$2.52 \cdot 10^{-17} \pm 5.00 \cdot 10^{-18}$	10
			$1.20 \cdot 10^3$	$< 3.00 \cdot 10^{-17}$	5
			$2.01 \cdot 10^4$	$< 6.42 \cdot 10^{-20}$	5
			$3.55 \cdot 10^4$	$< 1.27 \cdot 10^{-20}$	5

**Table A.3.** Photometric data used in this study for the targets  $\alpha$  Tau and  $\beta$  And. The literature references are specified at the end of Table A.5.

$\alpha$ Tau			$\beta$ And		
$\lambda$ [ $\mu\text{m}$ ]	$\lambda F_\lambda$ [ $\text{Wm}^{-2}$ ]	ref.	$\lambda$ [ $\mu\text{m}$ ]	$\lambda F_\lambda$ [ $\text{Wm}^{-2}$ ]	ref.
$3.46 \cdot 10^{-1}$	$1.85 \cdot 10^{-10} \pm 3.51 \cdot 10^{-12}$	4	$3.46 \cdot 10^{-1}$	$5.38 \cdot 10^{-11} \pm 6.61 \cdot 10^{-13}$	4
$3.60 \cdot 10^{-1}$	$2.93 \cdot 10^{-10} \pm 0.00$	1	$3.60 \cdot 10^{-1}$	$9.17 \cdot 10^{-11} \pm 0.00 \cdot 10^{+00}$	1
$4.01 \cdot 10^{-1}$	$9.98 \cdot 10^{-10} \pm 1.90 \cdot 10^{-11}$	4	$4.01 \cdot 10^{-1}$	$3.11 \cdot 10^{-10} \pm 3.83 \cdot 10^{-12}$	4
$4.23 \cdot 10^{-1}$	$2.09 \cdot 10^{-9} \pm 3.47 \cdot 10^{-11}$	4	$4.23 \cdot 10^{-1}$	$6.60 \cdot 10^{-10} \pm 5.98 \cdot 10^{-12}$	4
$4.40 \cdot 10^{-1}$	$3.31 \cdot 10^{-9} \pm 0.00$	1	$4.40 \cdot 10^{-1}$	$1.08 \cdot 10^{-9} \pm 0.00$	1
$4.48 \cdot 10^{-1}$	$3.37 \cdot 10^{-9} \pm 6.40 \cdot 10^{-11}$	4	$4.48 \cdot 10^{-1}$	$1.07 \cdot 10^{-9} \pm 1.31 \cdot 10^{-11}$	4
$5.39 \cdot 10^{-1}$	$8.08 \cdot 10^{-9} \pm 1.53 \cdot 10^{-10}$	4	$5.39 \cdot 10^{-1}$	$2.72 \cdot 10^{-9} \pm 3.34 \cdot 10^{-11}$	4
$5.49 \cdot 10^{-1}$	$8.79 \cdot 10^{-9} \pm 1.21 \cdot 10^{-10}$	4	$5.49 \cdot 10^{-1}$	$2.94 \cdot 10^{-9} \pm 1.08 \cdot 10^{-11}$	4
$5.50 \cdot 10^{-1}$	$9.41 \cdot 10^{-9} \pm 0.00$	1	$5.50 \cdot 10^{-1}$	$3.14 \cdot 10^{-9} \pm 0.00$	1
$5.81 \cdot 10^{-1}$	$1.07 \cdot 10^{-8} \pm 2.04 \cdot 10^{-10}$	4	$5.81 \cdot 10^{-1}$	$3.59 \cdot 10^{-9} \pm 4.41 \cdot 10^{-11}$	4
$7.00 \cdot 10^{-1}$	$1.81 \cdot 10^{-8} \pm 0.00$	1	$7.00 \cdot 10^{-1}$	$6.12 \cdot 10^{-9} \pm 0.00$	1
$9.00 \cdot 10^{-1}$	$2.71 \cdot 10^{-8} \pm 0.00$	1	$9.00 \cdot 10^{-1}$	$9.65 \cdot 10^{-9} \pm 0.00$	1
1.24	$2.66 \cdot 10^{-8} \pm 4.75 \cdot 10^{-9}$	12	1.24	$9.33 \cdot 10^{-9} \pm 1.77 \cdot 10^{-09}$	12
1.25	$2.31 \cdot 10^{-8} \pm 0.00$	1	1.25	$8.68 \cdot 10^{-9} \pm 2.92 \cdot 10^{-10}$	7
1.25	$2.38 \cdot 10^{-8} \pm 0.00$	6	1.25	$9.20 \cdot 10^{-9} \pm 0.00$	6
1.66	$2.43 \cdot 10^{-8} \pm 3.80 \cdot 10^{-9}$	12	1.66	$8.80 \cdot 10^{-9} \pm 1.20 \cdot 10^{-09}$	12
2.16	$1.53 \cdot 10^{-8} \pm 1.97 \cdot 10^{-9}$	12	2.16	$5.06 \cdot 10^{-9} \pm 7.46 \cdot 10^{-10}$	12
2.20	$1.14 \cdot 10^{-8} \pm 0.00$	1	2.20	$4.83 \cdot 10^{-9} \pm 5.64 \cdot 10^{-11}$	7
2.20	$1.19 \cdot 10^{-8} \pm 0.00$	6	2.20	$3.92 \cdot 10^{-9} \pm 0.00$	6
3.40	$4.33 \cdot 10^{-9} \pm 0.00$	6	3.40	$1.87 \cdot 10^{-9} \pm 0.00$	1
3.50	$3.79 \cdot 10^{-9} \pm 9.27 \cdot 10^{-11}$	7	3.40	$1.74 \cdot 10^{-9} \pm 0.00$	6
3.50	$3.65 \cdot 10^{-9} \pm 9.27 \cdot 10^{-11}$	7	3.50	$1.56 \cdot 10^{-9} \pm 3.78 \cdot 10^{-11}$	7
4.20	$2.88 \cdot 10^{-9} \pm 7.96 \cdot 10^{-10}$	2	3.50	$1.45 \cdot 10^{-9} \pm 3.78 \cdot 10^{-11}$	7
4.90	$1.19 \cdot 10^{-9} \pm 1.30 \cdot 10^{-11}$	7	4.20	$9.54 \cdot 10^{-10} \pm 2.64 \cdot 10^{-10}$	2
4.90	$1.17 \cdot 10^{-9} \pm 1.30 \cdot 10^{-11}$	7	4.90	$4.73 \cdot 10^{-10} \pm 6.23 \cdot 10^{-12}$	7
5.00	$1.24 \cdot 10^{-9} \pm 0.00$	1	4.90	$4.65 \cdot 10^{-10} \pm 6.23 \cdot 10^{-12}$	7
5.00	$1.40 \cdot 10^{-9} \pm 0.00$	6	5.00	$4.75 \cdot 10^{-10} \pm 0.00$	1
$1.02 \cdot 10^1$	$1.52 \cdot 10^{-10} \pm 0.00$	1	5.00	$5.51 \cdot 10^{-10} \pm 0.00$	6
$1.02 \cdot 10^1$	$1.95 \cdot 10^{-10} \pm 0.00$	6	$1.02 \cdot 10^1$	$6.94 \cdot 10^{-11} \pm 0.00$	1
$1.10 \cdot 10^1$	$1.74 \cdot 10^{-10} \pm 4.81 \cdot 10^{-11}$	2	$1.02 \cdot 10^1$	$8.11 \cdot 10^{-11} \pm 0.00$	6
$1.20 \cdot 10^1$	$1.23 \cdot 10^{-10} \pm 2.46 \cdot 10^{-11}$	3	$1.10 \cdot 10^1$	$7.59 \cdot 10^{-11} \pm 1.40 \cdot 10^{-11}$	2
$1.98 \cdot 10^1$	$3.09 \cdot 10^{-11} \pm 5.70 \cdot 10^{-12}$	2	$1.20 \cdot 10^1$	$5.05 \cdot 10^{-11} \pm 1.01 \cdot 10^{-11}$	3
$2.50 \cdot 10^1$	$1.31 \cdot 10^{-11} \pm 2.61 \cdot 10^{-12}$	3	$1.98 \cdot 10^1$	$1.12 \cdot 10^{-11} \pm 2.07 \cdot 10^{-12}$	2
$2.74 \cdot 10^1$	$9.55 \cdot 10^{-12} \pm 2.64 \cdot 10^{-12}$	8	$2.50 \cdot 10^1$	$5.84 \cdot 10^{-12} \pm 1.17 \cdot 10^{-12}$	3
$6.00 \cdot 10^1$	$9.79 \cdot 10^{-13} \pm 1.96 \cdot 10^{-13}$	3	$2.74 \cdot 10^1$	$4.57 \cdot 10^{-12} \pm 1.26 \cdot 10^{-12}$	2
$1.00 \cdot 10^2$	$1.76 \cdot 10^{-13} \pm 3.52 \cdot 10^{-14}$	3	$6.00 \cdot 10^1$	$4.08 \cdot 10^{-13} \pm 8.16 \cdot 10^{-14}$	3
$3.50 \cdot 10^2$	$4.54 \cdot 10^{-15} \pm 7.02 \cdot 10^{-16}$	13	$1.00 \cdot 10^2$	$8.39 \cdot 10^{-14} \pm 1.68 \cdot 10^{-14}$	3
$4.50 \cdot 10^2$	$2.03 \cdot 10^{-15} \pm 4.00 \cdot 10^{-16}$	13	$1.20 \cdot 10^3$	$6.25 \cdot 10^{-17} \pm 1.00 \cdot 10^{-17}$	5
$1.20 \cdot 10^3$	$1.27 \cdot 10^{-16} \pm 1.50 \cdot 10^{-17}$	5	$1.20 \cdot 10^3$	$< 1.00 \cdot 10^{-16}$	9
$1.38 \cdot 10^3$	$5.62 \cdot 10^{-17} \pm 1.23 \cdot 10^{-17}$	8	$1.20 \cdot 10^3$	$5.87 \cdot 10^{-17} \pm 1.10 \cdot 10^{-17}$	10
$2.77 \cdot 10^3$	$1.51 \cdot 10^{-17} \pm 1.58 \cdot 10^{-18}$	8	$1.33 \cdot 10^4$	$< 2.02 \cdot 10^{-17}$	5
$2.00 \cdot 10^4$	$8.98 \cdot 10^{-20} \pm 1.50 \cdot 10^{-20}$	5	$2.01 \cdot 10^4$	$8.37 \cdot 10^{-20} \pm 0.00$	5
$2.01 \cdot 10^4$	$1.28 \cdot 10^{-19} \pm 0.00$	5	$2.80 \cdot 10^4$	$< 5.34 \cdot 10^{-19}$	5
$2.80 \cdot 10^4$	$< 5.34 \cdot 10^{-19}$	5	$3.55 \cdot 10^4$	$1.52 \cdot 10^{-20} \pm 0.00$	5
$3.55 \cdot 10^4$	$2.53 \cdot 10^{-20} \pm 0.00$	5	$6.14 \cdot 10^4$	$< 1.03 \cdot 10^{-20}$	5
$6.14 \cdot 10^4$	$< 1.32 \cdot 10^{-20}$	5	$6.97 \cdot 10^5$	$< 4.30 \cdot 10^{-19}$	5
$6.97 \cdot 10^5$	$< 4.30 \cdot 10^{-19}$	5			

**Table A.4.** Photometric data used in this study for the targets  $\alpha$  Cet and  $\beta$  Peg. The literature references are specified at the end of Table A.5.

$\alpha$ Cet			$\beta$ Peg		
$\lambda$ [ $\mu\text{m}$ ]	$\lambda F_\lambda$ [ $\text{Wm}^{-2}$ ]	ref.	$\lambda$ [ $\mu\text{m}$ ]	$\lambda F_\lambda$ [ $\text{Wm}^{-2}$ ]	ref.
$3.46 \cdot 10^{-1}$	$3.44 \cdot 10^{-11} \pm 5.67 \cdot 10^{-13}$	4	$3.46 \cdot 10^{-1}$	$3.36 \cdot 10^{-11} \pm 1.80 \cdot 10^{-12}$	4
$3.60 \cdot 10^{-1}$	$5.68 \cdot 10^{-11} \pm 0.00$	1	$3.60 \cdot 10^{-1}$	$5.95 \cdot 10^{-11} \pm 0.00$	6
$4.01 \cdot 10^{-1}$	$1.98 \cdot 10^{-10} \pm 3.27 \cdot 10^{-12}$	4	$3.60 \cdot 10^{-1}$	$6.23 \cdot 10^{-11} \pm 0.00$	1
$4.23 \cdot 10^{-1}$	$4.16 \cdot 10^{-10} \pm 5.70 \cdot 10^{-12}$	4	$4.01 \cdot 10^{-1}$	$2.16 \cdot 10^{-10} \pm 1.16 \cdot 10^{-11}$	4
$4.40 \cdot 10^{-1}$	$6.49 \cdot 10^{-10} \pm 0.00$	1	$4.23 \cdot 10^{-1}$	$4.42 \cdot 10^{-10} \pm 2.32 \cdot 10^{-11}$	4
$4.48 \cdot 10^{-1}$	$6.82 \cdot 10^{-10} \pm 1.13 \cdot 10^{-11}$	4	$4.40 \cdot 10^{-1}$	$6.99 \cdot 10^{-10} \pm 0.00$	6
$5.39 \cdot 10^{-1}$	$1.82 \cdot 10^{-9} \pm 3.00 \cdot 10^{-11}$	4	$4.40 \cdot 10^{-1}$	$6.61 \cdot 10^{-10} \pm 0.00 \cdot 10^{+00}$	1
$5.49 \cdot 10^{-1}$	$1.98 \cdot 10^{-9} \pm 2.01 \cdot 10^{-11}$	4	$4.48 \cdot 10^{-1}$	$7.17 \cdot 10^{-10} \pm 3.84 \cdot 10^{-11}$	4
$5.50 \cdot 10^{-1}$	$2.02 \cdot 10^{-9} \pm 0.00$	1	$5.39 \cdot 10^{-1}$	$2.01 \cdot 10^{-9} \pm 1.07 \cdot 10^{-10}$	4
$5.81 \cdot 10^{-1}$	$2.39 \cdot 10^{-9} \pm 3.95 \cdot 10^{-11}$	4	$5.49 \cdot 10^{-1}$	$2.15 \cdot 10^{-9} \pm 1.11 \cdot 10^{-10}$	4
$7.00 \cdot 10^{-1}$	$4.35 \cdot 10^{-9} \pm 0.00$	1	$5.50 \cdot 10^{-1}$	$2.24 \cdot 10^{-9} \pm 0.00$	6
$9.00 \cdot 10^{-1}$	$7.95 \cdot 10^{-9} \pm 0.00$	1	$5.50 \cdot 10^{-1}$	$2.08 \cdot 10^{-9} \pm 0.00$	1
1.24	$7.51 \cdot 10^{-9} \pm 9.90 \cdot 10^{-10}$	12	$5.81 \cdot 10^{-1}$	$2.53 \cdot 10^{-9} \pm 1.36 \cdot 10^{-10}$	4
1.25	$7.11 \cdot 10^{-9} \pm 0.00$	1	$7.00 \cdot 10^{-1}$	$5.53 \cdot 10^{-9} \pm 0.00$	6
1.25	$7.56 \cdot 10^{-9} \pm 2.40 \cdot 10^{-10}$	7	$7.00 \cdot 10^{-1}$	$5.48 \cdot 10^{-9} \pm 0.00$	1
1.66	$8.27 \cdot 10^{-9} \pm 1.39 \cdot 10^{-9}$	12	$9.00 \cdot 10^{-1}$	$1.17 \cdot 10^{-8} \pm 0.00$	6
2.20	$3.85 \cdot 10^{-9} \pm 0.00$	1	$9.00 \cdot 10^{-1}$	$1.15 \cdot 10^{-8} \pm 0.00$	1
2.20	$4.10 \cdot 10^{-9} \pm 4.63 \cdot 10^{-11}$	7	1.24	$1.45 \cdot 10^{-8} \pm 2.58 \cdot 10^{-09}$	12
3.40	$1.36 \cdot 10^{-9} \pm 0.00$	1	1.25	$1.20 \cdot 10^{-8} \pm 4.31 \cdot 10^{-10}$	7
3.40	$1.53 \cdot 10^{-9} \pm 0.00$	1	1.25	$1.10 \cdot 10^{-8} \pm 4.31 \cdot 10^{-10}$	7
3.50	$1.33 \cdot 10^{-9} \pm 4.36 \cdot 10^{-11}$	7	1.66	$1.34 \cdot 10^{-8} \pm 2.22 \cdot 10^{-09}$	12
3.50	$1.26 \cdot 10^{-9} \pm 4.36 \cdot 10^{-11}$	7	2.16	$8.27 \cdot 10^{-9} \pm 1.17 \cdot 10^{-09}$	12
4.20	$9.54 \cdot 10^{-10} \pm 1.76 \cdot 10^{-10}$	2	2.20	$6.51 \cdot 10^{-9} \pm 0.00$	1
4.90	$4.08 \cdot 10^{-10} \pm 9.49 \cdot 10^{-12}$	7	2.20	$6.98 \cdot 10^{-9} \pm 9.16 \cdot 10^{-11}$	7
4.90	$3.86 \cdot 10^{-10} \pm 9.49 \cdot 10^{-12}$	7	3.40	$2.42 \cdot 10^{-9} \pm 0.00$	1
5.00	$3.64 \cdot 10^{-10} \pm 0.00$	1	3.40	$2.56 \cdot 10^{-9} \pm 0.00$	1
5.00	$4.58 \cdot 10^{-10} \pm 0.00$	6	3.50	$2.25 \cdot 10^{-9} \pm 5.76 \cdot 10^{-11}$	7
$1.02 \cdot 10^1$	$5.17 \cdot 10^{-11} \pm 0.00$	1	3.50	$2.09 \cdot 10^{-9} \pm 5.76 \cdot 10^{-11}$	7
$1.02 \cdot 10^1$	$6.10 \cdot 10^{-11} \pm 0.00$	6	4.20	$1.51 \cdot 10^{-9} \pm 4.18 \cdot 10^{-10}$	2
$1.10 \cdot 10^1$	$5.25 \cdot 10^{-11} \pm 1.45 \cdot 10^{-11}$	2	4.90	$7.20 \cdot 10^{-10} \pm 1.22 \cdot 10^{-11}$	7
$1.20 \cdot 10^1$	$4.12 \cdot 10^{-11} \pm 8.24 \cdot 10^{-12}$	3	4.90	$6.69 \cdot 10^{-10} \pm 1.22 \cdot 10^{-11}$	7
$1.98 \cdot 10^1$	$8.52 \cdot 10^{-12} \pm 0.00$	2	5.00	$7.26 \cdot 10^{-10} \pm 0.00$	1
$2.50 \cdot 10^1$	$4.78 \cdot 10^{-12} \pm 9.57 \cdot 10^{-13}$	3	5.00	$8.26 \cdot 10^{-10} \pm 0.00$	6
$6.00 \cdot 10^1$	$3.38 \cdot 10^{-13} \pm 6.76 \cdot 10^{-14}$	3	$1.02 \cdot 10^1$	$9.94 \cdot 10^{-11} \pm 0.00$	1
$1.00 \cdot 10^2$	$6.69 \cdot 10^{-14} \pm 1.34 \cdot 10^{-14}$	3	$1.02 \cdot 10^1$	$1.24 \cdot 10^{-10} \pm 0.00$	6
$3.50 \cdot 10^2$	$1.80 \cdot 10^{-15} \pm 3.08 \cdot 10^{-16}$	13	$1.10 \cdot 10^1$	$1.00 \cdot 10^{-10} \pm 2.77 \cdot 10^{-11}$	2
$4.50 \cdot 10^2$	$7.33 \cdot 10^{-16} \pm 2.20 \cdot 10^{-16}$	13	$1.20 \cdot 10^1$	$6.82 \cdot 10^{-11} \pm 1.36 \cdot 10^{-11}$	3
$1.20 \cdot 10^3$	$3.75 \cdot 10^{-17} \pm 7.50 \cdot 10^{-18}$	5	$1.98 \cdot 10^1$	$1.95 \cdot 10^{-11} \pm 0.00$	2
$1.20 \cdot 10^3$	$1.46 \cdot 10^{-16} \pm 2.33 \cdot 10^{-17}$	9	$2.50 \cdot 10^1$	$8.29 \cdot 10^{-12} \pm 1.66 \cdot 10^{-12}$	3
$2.01 \cdot 10^4$	$7.62 \cdot 10^{-20} \pm 0.00$	5	$2.74 \cdot 10^1$	$6.61 \cdot 10^{-12} \pm 0.00$	2
$3.55 \cdot 10^4$	$6.25 \cdot 10^{-20} \pm 0.00$	5	$6.00 \cdot 10^1$	$5.95 \cdot 10^{-13} \pm 1.19 \cdot 10^{-13}$	3
$3.56 \cdot 10^4$	$< 1.43 \cdot 10^{-18}$	5	$1.00 \cdot 10^2$	$1.03 \cdot 10^{-13} \pm 2.06 \cdot 10^{-14}$	3
$6.14 \cdot 10^4$	$< 7.82 \cdot 10^{-21}$	5	$3.50 \cdot 10^2$	$3.09 \cdot 10^{-15} \pm 3.17 \cdot 10^{-16}$	13
$1.31 \cdot 10^5$	$< 1.01 \cdot 10^{-18}$	5	$4.50 \cdot 10^2$	$1.60 \cdot 10^{-15} \pm 1.80 \cdot 10^{-16}$	13
			$1.20 \cdot 10^3$	$5.75 \cdot 10^{-17} \pm 1.25 \cdot 10^{-17}$	5
			$1.20 \cdot 10^3$	$7.29 \cdot 10^{-17} \pm 1.22 \cdot 10^{-17}$	9
			$1.20 \cdot 10^3$	$7.37 \cdot 10^{-17} \pm 1.37 \cdot 10^{-17}$	10
			$7.00 \cdot 10^3$	$1.07 \cdot 10^{-18} \pm 5.14 \cdot 10^{-20}$	11
			$2.01 \cdot 10^4$	$1.25 \cdot 10^{-19} \pm 0.00$	5
			$3.55 \cdot 10^4$	$< 3.04 \cdot 10^{-20}$	5
			$6.14 \cdot 10^4$	$< 9.77 \cdot 10^{-21}$	5

**Table A.5.** Photometric data used in this study for  $\sigma$  Lib. The literature references are specified underneath the table.

$\sigma$ Lib		
$\lambda$ [ $\mu\text{m}$ ]	$\lambda F_\lambda$ [ $\text{Wm}^{-2}$ ]	ref.
$3.46 \cdot 10^{-1}$	$1.62 \cdot 10^{-11} \pm 5.96 \cdot 10^{-13}$	4
$3.60 \cdot 10^{-1}$	$2.82 \cdot 10^{-11} \pm 0.00$	6
$3.60 \cdot 10^{-1}$	$2.62 \cdot 10^{-11} \pm 0.00$	1
$4.01 \cdot 10^{-1}$	$9.69 \cdot 10^{-11} \pm 3.57 \cdot 10^{-12}$	4
$4.23 \cdot 10^{-1}$	$1.98 \cdot 10^{-10} \pm 6.70 \cdot 10^{-12}$	4
$4.40 \cdot 10^{-1}$	$3.08 \cdot 10^{-10} \pm 0.00$	1
$4.40 \cdot 10^{-1}$	$3.28 \cdot 10^{-10} \pm 0.00$	6
$4.48 \cdot 10^{-1}$	$3.24 \cdot 10^{-10} \pm 1.19 \cdot 10^{-11}$	4
$5.39 \cdot 10^{-1}$	$9.09 \cdot 10^{-10} \pm 3.35 \cdot 10^{-11}$	4
$5.49 \cdot 10^{-1}$	$9.77 \cdot 10^{-10} \pm 2.97 \cdot 10^{-11}$	4
$5.50 \cdot 10^{-1}$	$1.02 \cdot 10^{-9} \pm 0.00$	1
$5.50 \cdot 10^{-1}$	$1.08 \cdot 10^{-9} \pm 0.00$	6
$5.81 \cdot 10^{-1}$	$1.16 \cdot 10^{-9} \pm 4.26 \cdot 10^{-11}$	4
$7.00 \cdot 10^{-1}$	$2.60 \cdot 10^{-9} \pm 0.00$	1
$7.00 \cdot 10^{-1}$	$2.96 \cdot 10^{-9} \pm 0.00$	6
$9.00 \cdot 10^{-1}$	$5.35 \cdot 10^{-9} \pm 0.00$	1
$9.00 \cdot 10^{-1}$	$5.98 \cdot 10^{-9} \pm 0.00$	6
1.24	$5.19 \cdot 10^{-9} \pm 7.84 \cdot 10^{-10}$	12
1.25	$5.65 \cdot 10^{-9} \pm 0.00$	6
1.25	$5.20 \cdot 10^{-9} \pm 1.40 \cdot 10^{-10}$	7
1.66	$5.70 \cdot 10^{-9} \pm 9.13 \cdot 10^{-10}$	12
2.16	$3.35 \cdot 10^{-9} \pm 6.12 \cdot 10^{-10}$	12
2.20	$3.20 \cdot 10^{-9} \pm 0.00$	6
2.20	$3.06 \cdot 10^{-9} \pm 4.83 \cdot 10^{-11}$	7
3.40	$1.18 \cdot 10^{-9} \pm 0.00$	1
3.50	$1.03 \cdot 10^{-9} \pm 2.60 \cdot 10^{-11}$	7
3.50	$9.74 \cdot 10^{-10} \pm 2.60 \cdot 10^{-11}$	7
4.20	$6.02 \cdot 10^{-10} \pm 1.11 \cdot 10^{-10}$	2
4.90	$3.23 \cdot 10^{-10} \pm 7.76 \cdot 10^{-12}$	7
4.90	$3.11 \cdot 10^{-10} \pm 7.76 \cdot 10^{-12}$	7
5.00	$3.23 \cdot 10^{-10} \pm 0.00$	1
5.00	$3.60 \cdot 10^{-10} \pm 0.00$	6
$1.02 \cdot 10^1$	$3.51 \cdot 10^{-11} \pm 0.00$	1
$1.02 \cdot 10^1$	$4.42 \cdot 10^{-11} \pm 0.00$	6
$1.10 \cdot 10^1$	$6.32 \cdot 10^{-11} \pm 1.75 \cdot 10^{-11}$	2
$1.20 \cdot 10^1$	$3.55 \cdot 10^{-11} \pm 7.10 \cdot 10^{-12}$	3
$1.98 \cdot 10^1$	$2.14 \cdot 10^{-11} \pm 9.86 \cdot 10^{-12}$	2
$2.50 \cdot 10^1$	$3.69 \cdot 10^{-12} \pm 7.39 \cdot 10^{-13}$	3
$6.00 \cdot 10^1$	$3.00 \cdot 10^{-13} \pm 6.00 \cdot 10^{-14}$	3
$1.00 \cdot 10^2$	$6.84 \cdot 10^{-14} \pm 1.37 \cdot 10^{-14}$	3
$1.20 \cdot 10^3$	$3.02 \cdot 10^{-17} \pm 6.75 \cdot 10^{-18}$	10
$3.57 \cdot 10^4$	$< 4.54 \cdot 10^{-19}$	5
$6.14 \cdot 10^4$	$< 1.03 \cdot 10^{-20}$	5

<sup>1</sup> UBVRJIKLMNH Photoelectric Catalogue (Morel & Magnenat 1978), <sup>2</sup> The Revised AFGL (RAFGL) Catalogue (Price & Murdock 1983), <sup>3</sup> IRAS catalogue of Point Sources, Version 2.0, <sup>4</sup> Observations in the Geneva Photometric System 4 (Rufener 1989), <sup>5</sup> Radio continuum emission from stars (Wendker 1995), <sup>6</sup> Stellar Photometry in Johnson's 11-color system (Ducati 2002), <sup>7</sup> COBE DIRBE Point Source Catalog (Smith et al. 2004), <sup>8</sup> Cohen et al. (2005), <sup>9</sup> Dehaes et al. (2007) <sup>10</sup> IRAM observations (this article) <sup>11</sup> VLA observations (this article) <sup>12</sup> 2MASS All-Sky Catalog of Point Sources (Skrutskie et al. 2006) <sup>13</sup> CSO observations (this article)